

Manuscript Details

Manuscript number	GLOPLACHA_2016_413
Title	Interaction of polar and tropical influences in the mid-latitudes of the Southern Hemisphere during the Mi-1 deglaciation
Short title	Polar and tropical interaction during Mi-1
Article type	Research paper

Abstract

It is well-known from geologic archives that Pleistocene and Holocene climate is characterised by cyclical variation on a wide range of timescales, and that these cycles of variation interact in complex ways. However, it is rarely possible to reconstruct sub-precessional (<20 kyr) climate variations for periods predating the oldest ice-core records (c. 800 ka). Here we present an investigation of orbital to potentially sub-precessional cyclicity from an annually resolved lake sediment core dated to a 100-kyr period in the earliest Miocene (23.03–22.93 Ma) and spanning a period of major Antarctic deglaciation associated with the second half of the Mi-1 event. Principal component analysis (PCA) of sediment bulk density, magnetic susceptibility (MS), and CIELAB L* and b* with a resolution of ~10 years indicates two major environmental processes governing the physical properties records, which we interpret as changes in wind-strength and changes in precipitation. Spectral analysis of the principal components indicates that both processes are strongly influenced by obliquity (41 kyr). We interpret this 41-kyr cycle in wind strength and precipitation as related to the changing position and strength of the Southern Hemisphere westerly winds. Precipitation is also influenced by an 11-kyr cycle. The 11-kyr periodicity is potentially related to orbital cyclicity, representing the equatorial semi-precessional maximum insolation cycle. This semi-precession cycle has been identified in a number of records from the Pleistocene and Holocene and has recently been suggested to indicate that insolation in low-latitude regions may be an important driver of millennial-scale climate response to orbital forcing (Feretti et al., 2015). This is the first time this cycle has been identified in a mid-latitude Southern Hemisphere climate archive, as well as the first identification in pre-Pleistocene records. The 11-kyr cycle appears at around 23.01 Ma, which coincides with the initiation of a major phase of Antarctic deglaciation, and strengthens during the subsequent period of rapid ice decay. This pattern suggests that the westerly winds may have expanded north of 50°S at the height of Mi-1, excluding tropical influence from the Foulden Maar site, and subsequently contracted polewards in tandem with warming deep-sea temperatures and Antarctic deglaciation, allowing the advection of tropical waters further south.

Keywords	Southern Hemisphere palaeoclimate; early Miocene; Mi-1 event; orbital forcing; semi-precession; westerly winds
Corresponding Author	Bethany Fox
Corresponding Author's Institution	University of Waikato
Order of Authors	Bethany Fox, William D'Andrea, Gary Wilson, Daphne Lee, Jo-Anne Wartho
Suggested reviewers	Patricio Moreno, Lionel Carter

Highlights:

- The mid-latitudes of the Southern Hemisphere are characterised by cyclical variation on obliquity (41 kyr) and semi-precession (11 kyr) timescales during the earliest Miocene
- The obliquity-scale variability is attributed to polar influence and the semi-precessional-scale variability to tropical influence
- Semi-precessional frequencies do not appear until 23.01 Ma, corresponding to the onset of Antarctic deglaciation and reduced polar influence
- The interaction between polar and tropical influence in the mid-latitudes is interpreted to be related to the position and strength of the westerly wind belt

Interaction of polar and tropical influences in the mid-latitudes of the Southern Hemisphere during the Mi-1 deglaciation

B. R. S. Fox^a, W. J. D'Andrea^b, G. S. Wilson^c, D. E. Lee^d, J.-A. Wartho^e

a: School of Science, University of Waikato, Private Bag 3105, Hamilton 3240, New Zealand

5 b: Lamont-Doherty Earth Observatory, Columbia University, 61 Route 9W – PO Box 1000, Palisades, NY, USA

c: Department of Marine Science, University of Otago, PO Box 56, Dunedin 9054, New Zealand

d: Department of Geology, University of Otago, PO Box 56, Dunedin 9054, New Zealand

10 e: GEOMAR Helmholtz Centre for Ocean Research Kiel, Wischhofstrasse 1-3, D-24148 Kiel, Germany

Keywords: Southern Hemisphere palaeoclimate, early Miocene, Mi-1 event, orbital forcing, semi-precession, westerly winds

15

Abstract

It is well-known from geologic archives that Pleistocene and Holocene climate is characterised by cyclical variation on a wide range of timescales, and that these cycles of variation interact in complex ways. However, it is rarely possible to reconstruct sub-precessional (<20 kyr) climate variations for periods predating the oldest ice-core records (c. 800 ka). Here we present an investigation of orbital to potentially sub-precessional cyclicity from an annually resolved lake sediment core dated to a 100-kyr period in the earliest Miocene (23.03–22.93 Ma) and spanning a period of major Antarctic deglaciation associated with the second half of the Mi-1 event. Principal component analysis (PCA) of sediment bulk density, magnetic susceptibility (MS), and CIELAB L* and b* with a resolution of ~10 years indicates two major environmental processes governing the physical properties records, which we interpret as changes in wind-strength and changes in

20

25

precipitation. Spectral analysis of the principal components indicates that both processes are strongly influenced by obliquity (41 kyr). We interpret this 41-kyr cycle in wind strength and precipitation as related to the changing position and strength of the Southern Hemisphere westerly winds. Precipitation is also influenced by an 11-kyr cycle. The 11-kyr periodicity is potentially related to orbital cyclicity, representing the equatorial semi-precessional maximum insolation cycle. This semi-precession cycle has been identified in a number of records from the Pleistocene and Holocene and has recently been suggested to indicate that insolation in low-latitude regions may be an important driver of millennial-scale climate response to orbital forcing (Feretti et al., 2015). This is the first time this cycle has been identified in a mid-latitude Southern Hemisphere climate archive, as well as the first identification in pre-Pleistocene records. The 11-kyr cycle appears at around 23.01 Ma, which coincides with the initiation of a major phase of Antarctic deglaciation, and strengthens during the subsequent period of rapid ice decay. This pattern suggests that the westerly winds may have expanded north of 50°S at the height of Mi-1, excluding tropical influence from the Foulden Maar site, and subsequently contracted polewards in tandem with warming deep-sea temperatures and Antarctic deglaciation, allowing the advection of tropical waters further south.

Introduction

The Oligocene/Miocene (O/M) boundary bore witness to a significant transient glaciation of Antarctica known as Mi-1 (e.g., Wilson et al., 2008). This event, which lasted ~400 kyr from 23.28 to 22.88 Ma, is still poorly understood, at least in part due to the paucity of continuous, high-resolution sedimentary records. Obliquity and precession cycles have been identified in a number of benthic foraminiferal oxygen and carbon isotope records from ocean drilling sites across the O/M boundary (e.g., Paul et al., 2000; Billups et al., 2004; Liebrand et al., 2011; Beddow et al., 2016) and have been interpreted to represent orbital control of the Antarctic ice sheet. However, due to the limited resolution of marine records, sub-Milankovitch-scale cycles during Mi-1 have rarely been investigated.

Foulden Maar is an ancient crater lake of Oligocene/Miocene age located on the South Island of New Zealand (Figure 1). The crater is filled with ~100 m of annually laminated diatomite
55 interbedded with slumps and fine-grained turbidites (the “swirly beds” and “speckled beds” of Lindqvist and Lee, 2009, respectively). These lake sediments overlie volcanoclastic diatreme breccias and mass flows representing early post-eruptive slumping of the unstable crater walls (Fox et al., 2015). The degree of preservation of organic material and diatom frustules within the sediments is exceptional (e.g., Bannister et al., 2005; Lindqvist and Lee, 2009; Bannister et al.,
60 2012; Reichgelt et al., 2013; Kaulfuss et al., 2014; Reichgelt et al., 2016). A combination of radiometric and magnetic techniques has been used to constrain the period of sediment deposition to 23.03–22.93 Ma (Fox et al., 2016). The sediments thus accumulated in Foulden Maar during the first ~100,000 years of the Miocene, corresponding with the deglaciation phase of the Mi-1 event (e.g., Miller et al., 1991, Wilson et al., 2008). Foulden Maar is the highest-resolution record of the
65 earliest Miocene, as well as the only record we know of from the terrestrial mid-latitudes of the Southern Hemisphere.

Paleobotanical studies indicate that at the end of its depositional period, the lake had a small, heavily forested catchment area with a seasonally dry and warm-temperate climate and very high levels of annual precipitation, estimated at 1700–2000 mm per year (Reichgelt et al., 2013). Four
70 main facies have been described in the lake sediment succession: white laminated diatomite (WLDA), dark laminated diatomite (DLDA), turbidites, and slumps (Fox et al., 2016). Based on stratigraphical considerations, slumps, turbidites and diatomaceous breccia are inferred to represent instantaneous resedimentation of material from shallow toward deeper zones within the lake, and all data in this study are presented with these intervals removed (Fox et al., 2016). WLDA and DLDA
75 differ mainly in the thickness and colour of their diatom-rich layers.

Fox et al. (2016) examined physical properties (density, CIELAB L* and a* reflectance, and RGB data) from the Foulden Maar deposit. They observed a strong ~41-kyr signal in the sediment density, a*, and red intensity records that they attributed to obliquity-driven climate forcing, and a

~23-kyr signal in the L* records that they attribute to precession-driven climate forcing. Here, we
80 build on this previous work in two ways: first, we examine sub-precessional variability in the
physical properties and identify a number of cycles, in particular a semi-precessional 11-kyr cycle;
and second, we perform a more detailed statistical analysis of the physical properties dataset to
elucidate the forcing factors behind the orbital and sub-orbital cycles identified. In the
supplementary material, we also report revised error calculations for the $^{40}\text{Ar}/^{39}\text{Ar}$ dates on which
85 the Foulden Maar age model is based.

Methods

We measured density, magnetic susceptibility, L* and b* using a Geotek Multi-Sensor Core Logger
(Geotek Ltd., 2014). Density and magnetic susceptibility were measured at 0.5 cm intervals on split
90 core. Density was measured by gamma attenuation using a cesium-137 source and calibrated at the
beginning and end of each measurement session using a custom-made aluminium calibration piece.
Magnetic susceptibility was measured using a Bartington Instruments MS2E point sensor calibrated
to a standard by Geotek technicians. L* and b* were measured at 1 cm intervals using the Geotek
spectrophotometer. The spectrophotometer was calibrated using the white calibration piece
95 provided. We carried out our measurements on the split face of core FH2 within a few months of
drilling operations.

Because magnetic susceptibility varies with temperature, cores were stored at room temperature
for at least twenty-four hours prior to analysis and temperature was monitored for drift during the
measurement period. We found that the temperature varied by $<1^\circ\text{C}$ within any given measurement
100 session, and the total temperature range across all sessions was 3.6°C . The magnetic susceptibility
sensor was zeroed after every ten measurements.

After measurement, we found that the density data show a large step change at ~49 m depth
(Supplementary Figure 1). This step occurs at the transition between one core section and the next.
We assumed this step to be an artefact and corrected for it by splitting the dataset at the step,

105 normalising each half of the dataset separately, and then recombining and detrending the combined
dataset. All statistical analyses presented in this paper were run on the corrected dataset. However,
statistical analyses run on the uncorrected dataset are presented in the supplementary material for
completeness (Supplementary Figures 2–3). The minor differences in these analyses do not affect
the conclusions presented here.

110 Samples for total organic carbon (TOC) analysis were taken by homogenising sediment
representing ~2000-year intervals throughout the core, excluding non-laminated material. The
stratigraphic thickness of these intervals ranged from 1.1 to 3.8 m. Samples were freeze-dried and
homogenized prior to being weighed and packed into tin capsules for TOC analysis on a Costech
elemental combustion system (EA). Calibration curves for calculating the instrument response to
115 known masses of carbon were generated using a series of acetanilide standards. Pooled standard
deviations of replicate measurements were used to calculate measurement uncertainty.

Spectral analysis was conducted using the SSA-MTM Toolkit v 4.4 to perform Blackman-
Tukey analyses with a window length of $0.3N$ (Dettinger et al., 1995; Ghil et al., 2002). For wavelet
analysis, we used the MATLAB scripts provided by Torrence and Compo (1998). Principal
120 component analysis (PCA) was performed using the `prcomp` function in R, with data both zero-
centred and unit-scaled before analysis (Venables and Ripley, 2002). In order to allow easier
comparison between the low-resolution TOC record and the higher-resolution physical properties
records, we averaged the physical properties records across the same time intervals as those
represented by the TOC samples. These averaged timeseries are here referred to as the resampled
125 dataset.

Results

Spectral analysis of physical properties and TOC

Figure 2 shows the four physical properties and TOC data, along with the 2000-yr resampled
130 physical properties data to allow easier comparison with TOC. Blackman-Tukey spectra of density,

magnetic susceptibility, b^* , and L^* are shown in Figure 3. Density and b^* show significant peaks at the 41 kyr period, corresponding to obliquity, while L^* has a prominent peak at 23 kyr, corresponding to precession. In the sub-precession band, both density and magnetic susceptibility indicate spectral power at around 11 kyr. Magnetic susceptibility and b^* have power at around 15 kyr. b^* has power at around 5.5 kyr, which corresponds to a peak that falls just below the AR(1) spectrum in the L^* record.

Given that the 11-kyr cycle is half the length of the precessional cycle, it is possible that it may be an artefact of the Blackman-Tukey statistical processing. In order to exclude this possibility, we bandpass-filtered the physical property time series for frequencies between 1/500 and 1/15,000 years. The results are shown in Figure 4a–d, and indicate that the 11-kyr cycle is a robust feature of the density, MS and b^* records, while the L^* record shows a periodicity closer to 15 kyr.

Figure 5 shows wavelet spectra for L^* , b^* , density, and MS (interpolated at 10-year intervals). Wavelet and Blackman-Tukey results broadly agree, although it must be borne in mind that edge effects are possible outside the “cone of influence” of the wavelet plot (Torrence and Compo, 1998), and therefore comparison to Blackman-Tukey results in this region should be made with caution. Of the sub-precessional cycles present, the 11-kyr cycle in the density record is the most clearly defined. It is less persistent in the MS record, disappearing at ~ 22.96 Ma. The ~ 15 -kyr cycle appears in the MS and b^* records, but again disappears in the MS record after ~ 22.96 Ma. There is also some evidence for this cycle in the L^* record, which may be obscured in the Blackman-Tukey results by the breadth of the peak centred on 23 kyr. The ~ 5.5 -kyr cycle appears in the earlier part (23.02–22.97 Ma) of the MS record and the later part (22.98–22.93 Ma) of the b^* record.

Principal components analysis

Figure 6 shows the results of PCA for the full dataset for density, MS, L^* , and b^* (Figure 6a, b), and for the 2000-yr resampled dataset (Figure 6c, d), which includes TOC. In the former, the first three principal components (PCs) explain 91% of the variance, and in the latter the first three PCs

explain 90% of the variance. Table 1 shows the component loadings for each variable for the first three principal components of both the full and the resampled datasets. Figure 7 shows the reconstructed PCs for both the full and resampled dataset as timeseries. A comparison of the reconstructed principal components timeseries with the original variables for each principal component can be found in Supplementary Figures 4–9.

The first principal component (PC1) of the full dataset explains 44.7% of the variance. It is weakly positively correlated with density and MS and strongly negatively correlated with L* and b* (Table 2). Detailed comparisons between the reconstructed timeseries of PC1 and the original variables indicate that these correlations apply throughout the depositional period (Supplementary Figure 4). PC1 of the resampled dataset shows a similar pattern of relatively weak positive correlation with density and stronger negative correlation with L* and b*, but also shows a stronger positive correlation with magnetic susceptibility and TOC (Table 2, Supplementary Figure 7). A comparison of PC1 of the full dataset with PC1 of the resampled dataset shows that they are similar in shape, suggesting that they are likely to represent the same or similar environmental processes (Figure 8).

PC2 in the full dataset explains 26.4% of the variance and is strongly positively correlated with density, positively correlated with MS and L*, and weakly positively correlated with b* (Table 1). A comparison of the reconstructed timeseries of PC2 with the physical properties records indicates that PC2 closely resembles density and (to a lesser extent) MS (Supplementary Figure 5). PC3 in the full dataset (representing 20.1% of the overall variance) is strongly negatively correlated with density, strongly positively correlated with MS, and shows little correlation with b* or L*. The reconstructed timeseries shows a strong resemblance to both density and MS (Supplementary Figure 6).

PC2 of the resampled dataset is strongly positively correlated with density and negatively correlated with MS (Table 1). Comparison of the reconstructed PC timeseries with the original variables shows a clear relationship in the case of density, but no very obvious relationship in the

case of MS (Supplementary Figure 8). PC3 of the resampled dataset is strongly positively correlated with both L* and magnetic susceptibility, but only weakly positively correlated with b*, density and TOC (Table 1). The relationship between the reconstructed timeseries and the original variables is not clear-cut (Supplementary Figure 9).

Figure 9 shows Blackman-Tukey analyses of PCs 1–3 for the full dataset. The 41-kyr obliquity cycle appears in all three PCs. Of the three sub-precessional cycles that occur in the proxy records, two are represented here: the 15 kyr cycle in PC1 (Figure 9a) and the 11 kyr cycle in PC2 (Figure 9b). The ~6 kyr cycle does not appear. PC3 has a broad peak between ~10 and ~20 kyr (Figure 9c).

Discussion

Principal components as proxies for compositional variability

PC1 is strongly negatively correlated with L* and b*. L* represents brightness, with 100 being pure white and 0 being black, and b* represents a spectrum from blue to yellow, with bluer hues represented by negative numbers and yellower hues by positive numbers. L* is often related to the carbonate concentration of sediments (e.g., Schneider et al., 1995), and is also affected by the presence of white minerals such as some clays (Balsam et al., 1999; Debret et al., 2006). The Foulden Maar sediments are non-calcareous and clay-poor, and the sediment brightness and hue (i.e., L* and b*) are primarily determined by the relative concentrations of diatom frustules vs. organic matter. Within the white laminated diatomite facies, the dark organic-rich laminae do not vary much in thickness; instead, variations in the thickness of light diatom-rich laminae determine couplet thickness and overall sediment hue, and therefore represent the first order control on both L* and b*. The particularly strong anticorrelation of TOC vs L* and b* on the PC1 axis suggests that PC1 represents sediment appearance, which primarily reflects biogenic silica (BSi) sedimentation rate.

BSi and organic matter both have low densities compared to mineral grains (excluding clay minerals). Thus, changes in density in the Foulden Maar sediments can be understood in relation to

the proportion of (non-clay) minerogenic sediment. Magnetic susceptibility is also commonly used
210 as a measure of minerogenic content, since biogenic sediments are diamagnetic while most
minerogenic sediments contain some fraction of paramagnetic or ferrimagnetic material. The
proportion of minerogenic sediment in the Foulden Maar diatomite is very low (Lindqvist and Lee,
2009; Fox et al., 2015, 2016). The relatively weak positive correlation of minerogenic indicators
with PC1 in the full dataset may be due to a dilution factor, with increased BSi sedimentation
215 leading to dilution of the minor minerogenic fraction. Given the weakness of the correlation and the
very low proportion of minerogenic material, it is unlikely to indicate the opposite case of increased
minerogenic input diluting the BSi content.

PC1 of the resampled dataset shows a divergence between density and MS, with MS more
strongly positively correlated and density showing a relatively weak correlation. This divergence is
220 difficult to understand if we consider both MS and density as simple measures of the proportion of
minerogenic material. The resampled MS dataset also correlates well with the TOC dataset
(correlation coefficient of 0.695, vs. 0.254 for density with TOC).

There are two potential explanations for these observations. The first is that variability in MS is
primarily controlled by the concentration of paramagnetic clays rather than ferrimagnetic minerals.
225 Since clays are less dense than most other minerogenic material, MS would then diverge from
density. Clays also tend to form complexes with organic matter, explaining the correlation between
MS and TOC.

The second possibility is related to the composition of the magnetic fraction, which was
inferred in Fox et al. (2015) to be primarily pyrrhotite. Iron sulphide minerals such as pyrite and
230 pyrrhotite have a strong affinity to organic carbon (Morel and Hudson, 1985; Muramoto et al.,
1991; Lalonde et al., 2012). While all minerogenic particles are likely to adsorb a certain amount of
organic matter, ferrous-iron-bearing minerals can form complexes with high ratios of organic
carbon to iron (Lalonde, 2012). Fine (nanoscale) particles of ferrous-iron-bearing phases in the
water column will be strongly attracted to sinking organic matter; thus, in certain specific

235 circumstances of reducing conditions, organic carbon will effectively scavenge fine particles of iron
as it is deposited (e.g., Muramoto et al., 1991). This interaction is not observed with less strongly-
binding silicate minerals such as those that characterise both schist and basalt and may be expected
to form the bulk of the minerogenic fraction in the Foulden Maar sediment (Graham and Mortimer,
1992; Adams and Robinson, 1993; Forsyth, 2001).

240 It may therefore be possible to understand the correlation between MS and TOC in terms of the
interaction between organic carbon and either clay minerals or fine ferrimagnetic iron sulphide
particles (or both). If this is the case, it suggests that MS is ambiguous as a proxy for minerogenic
input to the lake basin.

Density is a measure of the overall (non-clay) minerogenic proportion, rather than just the
245 magnetic fraction. Silicate grains such as quartz and feldspar do not exhibit the complexing
behaviour of Fe(II)-bearing phases, and so will not be strongly scavenged by sinking organic
matter. Thus, we interpret density as a more straightforward measure of the input of minerogenic
material to the lake system. We interpret the variability of MS along the PC1 axis as a combination
of dilution by BSi and concentration by interaction with organic carbon, and the variability of
250 density as dominated by the dilution effect.

The moderate to strong positive correlation of density and MS with PC2 indicates that the
process this PC represents must be one that exerts a major control on minerogenic content. The
weaker but still positive correlation of L^* and b^* to this PC means the process cannot be related to
dilution by BSi. This can be understood as changes in the minerogenic sedimentation rate. Given
255 the very small minerogenic component, an increase in minerogenic sedimentation rate will not be
enough to appreciably dilute the BSi. PC3 of the resampled dataset shows a similar pattern of
positive correlation with all records, but the strength of the correlations is quite different, with a
substantial reduction in the strength of the correlation with density and increase in the strength of
the correlation with L^* . It is possible that this represents a similar environmental process to PC2 of
260 the full dataset, but given the changes in correlation strength as well as the lack of a clear

relationship between the reconstructed PC timeseries and the original physical properties, this conclusion is speculative. We do not attempt to further interpret PC3 of the resampled dataset here.

PC3 of the full dataset shows a strong anticorrelation between density and MS, again indicating that these properties cannot both be interpreted as simple proxies for minerogenic content. PC2 of the resampled dataset shows a similar anticorrelation between density and MS, with only very weak correlations with the other three records. The process represented by these two PCs is not straightforward to interpret, but given the low density and often paramagnetic nature of clay minerals, it may be related to variability in the proportion of clay vs silt- to sand-sized minerogenic material in the sediment. However, given the lack of further data to confirm or refute this hypothesis, and the relatively low proportion of variance explained, we make no attempt to further interpret these PCs here.

Principal components and environmental processes

The principal components analysis indicates three major environmental processes: one which is closely related to variability in diatom productivity (PC1 of both datasets), one related to variability in minerogenic input (PC2 of the full dataset and perhaps PC3 of the resampled dataset) and a third process which may be related to variability in the proportion of clay vs silt/sand-sized particles (PC3 of the full dataset and PC2 of the resampled dataset). The nature of these environmental processes remains to be understood.

Diatom productivity in lakes may be limited by ice cover, surface-water temperature, wind-mixing, and nutrient and silica availability, the latter of which may in turn be affected by wind-mixing and/or precipitation (Round et al., 1990). Sediment input through aeolian, fluvial, or run-off processes may also play a role in both light availability (turbidity) and nutrient availability. Climatic parameters at Foulden Maar at the end of the depositional period, as estimated using the climate leaf analysis multivariate programme (CLAMP) and bioclimatic analysis, indicate a climate that was warm-temperate and very humid, with a large seasonal variability in precipitation (Reichgelt et al.,

2013). Given the equable temperature regime and inferred low-lying, maritime location, it is unlikely the lake was ever ice-covered for any appreciable period of time. There is also no evidence for any fluvial input into the Foulden Maar basin (i.e., it was a closed-basin lake).

290 In order to establish the most likely controls on diatom productivity at Foulden Maar, we examined a number of studies of modern closed-basin maar lakes from varying climatic regimes and geographic settings. These include Lake Pupuke, a modern Auckland maar lake in a warm-temperate climate regime and maritime setting (Striewski et al., 2009; Striewski et al., 2013); Sihailongwan and Erlongwan, two seasonally ice-covered maar lakes in a monsoonal regime in
295 North-East China (Chu et al., 2002; Chu et al., 2005; Schettler et al., 2006; Wang et al., 2012); and Huguang Maar, located in a low-lying, coastal, tropical region of South China (Lu et al., 2003; Mingram et al., 2004).

Despite the variability in conditions at these modern sites, diatom productivity in all four of these modern maar lakes is considered to be closely related to nutrient availability. Two main
300 controls on nutrient availability are invoked in these studies: wind-speed (related to overturn of the lake and upward mixing of nutrient-rich waters) and precipitation (related to influx of nutrient-rich groundwater). At Foulden Maar, the proxies for minerogenic input (density, MS) are found to have an inverse relationship with proxies for diatom productivity (L^* , b^*) along the PC1 axis. This suggests that PC1 is unlikely to be related to increased precipitation, as we would expect this to lead
305 to increased minerogenic input. While there may be some element of temperature limitation, by analogy with similar modern maar lakes we propose that PC1 is primarily related to changes in wind-strength.

PC2 of the full dataset is here interpreted to primarily reflect variation in minerogenic input to the lake. These changes are very small, as evidenced by the low absolute values of both density and
310 magnetic susceptibility (Figure 2). Minerogenic input may increase through increased erosion of the catchment (increased precipitation) or increased aeolian sedimentation (increased wind strength and/or decreased vegetation cover in source areas). Increased wind strength would also have the

effect of increasing wind mixing in the lake as well as potentially introducing micronutrients via wind-blown dust, both of which would increase diatom productivity. We consider that the relatively
315 weak positive correlation of L^* and especially b^* with this axis makes it unlikely that changes in wind strength are the primary process controlling PC2. We therefore interpret this axis as most likely to be related to changes in precipitation, and thus in catchment erosion. The weak positive correlation of the productivity indicators may be a result of increased influx of nutrient-rich groundwater to the lake during wetter intervals, as observed in the Chinese maar lakes (Chu et al.,
320 2002; Chu et al., 2005; Wang et al., 2012). The low magnitude of the variability in minerogenic input is to be expected in a small lake with a very limited catchment area (most likely restricted to the tephra rim that is inferred to have originally surrounded the lake).

The 41-kyr cycle

325 41-kyr cycles identified with obliquity have been found in a number of deep-ocean records across the O/M boundary, most clearly in oxygen and carbon isotope records from ODP Sites 926 (equatorial Atlantic, Pälike et al., 2006a) and 1090 (Southern Ocean, Atlantic sector, Billups et al., 2004). The 41-kyr obliquity cycle also appears in wavelet analyses of oxygen and carbon isotope records from Site 1218 (Pälike et al., 2006b) and Site U1334 (Beddow et al., 2016), both tropical
330 Pacific, although it is relatively weak during Mi-1.

The interpretation of oxygen isotope records can be difficult, as they are influenced by both water temperature and land-ice volume, and inverse modelling suggests that the contributions of these two components vary widely across the Cenozoic (De Boer et al., 2010). For the O/M boundary, some studies have attempted to solve this problem using independent estimates of water
335 temperature (Mg/Ca, Lear et al., 2004; Mawbey and Lear, 2013). These studies indicate that ice growth and decay contribute a major proportion of the oxygen isotope signal across Mi-1, and indicate that the extent of global land ice was at least partly paced by obliquity.

However, the 41-kyr cycle does not appear clearly in all O/M boundary oxygen isotope records,

as would be expected if it were a truly global signal: it is only weakly observed at Site 1264
340 (subtropical South Atlantic, Liebrand et al., 2011, 2016). Beddow et al. (2016) proposed that this
was either due to the shallow location of 1264 (suggesting that the polar signal was transmitted
through the movement of deep water masses) or the low sedimentation rate at the site.

In our record, the appearance of the 41-kyr cycle in both the PC1 and PC2 spectra indicates that
both wind strength and precipitation at the lake site are affected by obliquity. The major wind-field
345 in the mid-latitudes of the Southern Hemisphere is the westerly wind belt. In the Pleistocene and
Holocene, the position and strength of the westerly winds are known to vary on both short and long
timescales, and are affected by a range of climate phenomena, including the meridional temperature
gradient, the southern annular mode (SAM) and the strength of tropical influence, in particular the
El Niño-Southern Oscillation (ENSO) (Stewart et al., 1984; Moreno et al., 2004; Shulmeister et al.,
350 2004; Gomez et al., 2012). The westerly winds also have an effect on precipitation, with areas in the
core of the westerly wind belts experiencing higher levels of precipitation than areas with lower
wind speeds, and increases in intensity of the winds leading to increased precipitation in these
regions (Moreno et al., 2004; Moreno et al., 2010). Although the boundary conditions at the O/M
boundary were quite different from those of the present day, the presence of an isolated, glaciated
355 polar continent seems likely to have produced a westerly wind belt with at least some of the same
characteristics. We therefore propose that the variability in wind strength and precipitation we infer
from our record is related to changes in the position and strength of the westerly winds, and that
these changes are partly paced by obliquity.

360 *The 11-kyr cycle*

The origin of the 11-kyr cycle is less clear-cut than that of the 41-kyr cycle. An 11-kyr cycle in
maximum summer insolation has been identified in the equatorial region. This cycle is caused by
the coincidence of perihelion with the vernal or autumnal equinox, which occurs twice during each
precession cycle (Short et al., 1991; Berger and Loutre, 1997; Berger et al., 2006; Ashkenazy and

365 Gildor, 2008). This halving of precession has been noted in Pleistocene and Holocene paleoclimate
archives for tropical paleolatitudes and for records that are affected by tropical signals, such as the
monsoon and atmospheric methane records (e.g., Pokras and Mix, 1987; Hagelberg et al., 1994;
Yiou et al., 1995; Delmotte et al., 2004), but also in reconstructions of atmospheric circulation
derived from glaciochemical proxies in ice cores (e.g., Mayewski et al., 1997). It has also recently
370 been identified in a mid-latitude North Atlantic record from the Pleistocene, and has been suggested
to indicate that low-latitude insolation may be an important driver of millennial-scale variability in
extratropical regions (Feretti et al., 2015). The mechanism is still not well understood, although
Feretti et al. (2015) suggest that it may relate to advective transport of waters polewards from the
tropics, perhaps in response to changes in the polar fronts.

375 The appearance of an 11-kyr cycle in the Foulden Maar core adds further support to the
suggestion that tropical insolation plays a part in mid-latitude climate, indicating that it may also
have been of importance at the beginning of the Neogene. Previous studies have inferred a role for
the 11-kyr cycle in controlling wind-speed (Pokras and Mix, 1987), low-latitude precipitation
(Hagelberg et al., 1994), mid-latitude temperature (Hagelberg et al., 1987), temperature/ice volume
380 (Feretti et al., 2015), and tropical methane emissions (Delmotte et al., 2004). Our results indicate
that the 11-kyr cycle may also have an effect on mid-latitude Southern Hemisphere precipitation
patterns.

The 15-kyr cycle

385 The 15-kyr cycle that appears in PC1 (Figure 9) does not correspond to any global climate cycles
that we are aware of. It is likely that it is related to the appearance of intervals of dark laminated
diatomite (DLDA, Fox et al., 2016) in the sediment. Such intervals have higher MS and lower L*
and b*. Five major intervals of DLDA appear in the Foulden Maar core (Table 2). With the
exception of the lowermost interval, the approximate spacing between these DLDA intervals is ~15
390 kyr (Table 2). However, if this were a true regular cycle, further DLDA intervals would be expected

to occur at depths of ~27 and ~15 m in the deposit (22.963 and 22.948 Ma, respectively). These intervals are not present, and, given this lack and the small number of DLDA intervals (4) that fit a regular pattern, it is not implausible that this ~15-kyr cyclicity is coincidental. The identification of the 15-kyr cyclicity in L*, b* and MS records with the DLDA intervals may be further supported by
395 the disappearance of this cyclicity above ~27 m depth (22.96 Ma) in the core in the MS record, coinciding with the disappearance of the DLDA intervals (Figure 5). However, all other significant cycles also disappear in the MS record above this point, while the ~15-kyr cycle continues, albeit at lower power, in both the L* and b* records. At present, the origins of and controls on the DLDA intervals are undetermined; however, further investigation may throw light on these, and thus on the
400 significance of the apparent 15-kyr cyclicity.

Interaction between polar and tropical influences in the mid-latitudes of the Southern Hemisphere during the Mi-1 deglaciation

The two major significant cycles present at Foulden Maar are above interpreted as related to the
405 position and strength of the westerly winds (41 kyr) and variability in equatorial insolation (11 kyr). In the present day, the position and strength of the westerly winds are an expression of the balance between the polar and tropical regions. For example, they expanded northwards during the last glacial maximum and contracted southwards in the warm period immediately following this (Stewart et al., 1984), and they have broadly increased in strength with increasing meridional
410 temperature gradient since that time (Renssen et al., 2005). In recent years, there has been some indication that global warming and/or ozone depletion is producing an increase in the SAM, leading to a poleward shift of the westerlies (Kushner et al., 2001; Roemmich et al., 2007), an increase in the intensity of the subtropical South Pacific gyre (Cai, 2006) and increased advection of warm tropical waters to the Southern Hemisphere mid-latitudes (Hill et al., 2008).

415 Figure 5a and b indicate that, in the density and magnetic susceptibility records, the 11-kyr cycle does not appear until around 23.01 Ma, and reaches its maximum power around 22.99–22.98

Ma. This coincides with a major Antarctic ice-decay event reconstructed by Mawbey and Lear (2013), beginning at about 23.01 Ma and continuing until around 22.97 Ma. The onset and peak of influence from the 11-kyr cycle in our record correspond to the initiation and most rapid period of ice-decay, respectively. Subsequent to this period of rapid ice-sheet decay, Mawbey and Lear (2013) reconstruct a period of minor ice-sheet growth.

We interpret this pattern to indicate the interaction of polar and tropical influences at the Foulden Maar site. During the initial phase of the depositional period, when the Antarctic ice-sheet was large (23.03–23.01 Ma), tropical influence was excluded from the site, perhaps due to an increased meridional temperature gradient and northwards expansion of the westerly winds. During the second phase (23.01–22.96 Ma), the ice-sheet underwent rapid decay, which would have coincided with reduced Antarctic influence, a southwards contraction of the westerly winds, and the introduction of tropical influence to the site of Foulden Maar, perhaps via advection of tropical waters southwards, as suggested by Feretti et al. (2015) for MIS19 and observed in the present day (Hill et al., 2008). The subsequent more minor expansion of the ice-sheet (22.96–22.93 Ma) might be expected to coincide with a reduction in tropical influence and in the significance of the 11-kyr cycle at the Foulden Maar site. However, although such a reduction is apparent in the MS record (Figure 5b), there is also a node in the equatorial maximum insolation cycle at this time (Figure 4e), and so no conclusions can be drawn here regarding tropical and polar interaction.

A recent study used palaeobotanical evidence from Foulden Maar to reconstruct a major increase in atmospheric carbon dioxide in the early Miocene at around 23.01–22.99 Ma (Reichgelt et al., 2016). One potential cause of this increase in CO₂ was suggested to be a southward shift of the westerly wind belt, resulting in enhanced oxidation of organic carbon. This is consistent with our interpretation of a southward shift of the westerly wind belt leading to the onset of tropical influence on the site at around 23.01 Ma. However, we note that there are a number of other potential causes for changes in atmospheric CO₂ which do not presuppose changes in the position of the westerlies, and thus this interpretation must be considered speculative.

Conclusions

445 The Foulden Maar core is a uniquely high-resolution record of the deglaciation phase of the Mi-1 event, and provides the first opportunity to reconstruct sub-precessional climate cycles and their influence on the mid-latitudes of the Southern Hemisphere at this time. Spectral and principal component analyses indicate cycles at 41, 15 and 11 kyr in the patterns of minerogenic input (precipitation) and overall diatom productivity (wind-strength). The origin of the 15-kyr cycle is not
450 clear, and it may be coincidental. The 11-kyr cycle is inferred to be related to the tropical semi-precessional maximum insolation cycle, which is known from Pleistocene and Holocene records, although it is not widely discussed. This cycle has recently been identified in Pleistocene North Atlantic oxygen isotope records and been interpreted as an indication that insolation in low-latitude regions may play an important role in the extra-tropical millennial-scale response to orbital forcing
455 (Feretti et al., 2015). The identification of the 11-kyr cycle in the mid-latitude Foulden Maar deposit supports this suggestion and indicates that low-latitude insolation may also have played an important role in the early Miocene.

During the Mi-1 deglaciation, the mid-latitude Foulden Maar site was affected by the changing strength and position of the westerly winds, which were primarily paced by obliquity. Obliquity has
460 also been proposed as a control on Antarctic ice volume during the second half of Mi-1 (e.g., Beddow et al., 2016), and the shifting of the westerly winds may be interpreted as an expression of the shifting balance between polar and tropical influences. The 11-kyr cycle was not apparent during the early phase of extensive Antarctic glaciation (23.03–23.01 Ma), and this may indicate that at this time the westerlies has expanded northwards and were excluding tropical influence from
465 the Foulden Maar site. The 11-kyr cycle reached maximum power during a phase of major ice decay (23.01–22.96 Ma), again indicating interaction between polar and tropical influences. The power of the 11 kyr cycle is reduced during a phase of minor ice-sheet growth (22.96–22.93 Ma) and presumably reduced Antarctic influence. However, this reduction in power also coincides with

a node in the equatorial maximum insolation cycle, and the contributions of these two factors to the
470 reduction in power cannot be assessed. Overall, millennial- to orbital-scale cycles in the Foulden
Maar core indicate a shifting balance of power between tropical and polar influences in the mid-
latitudes of the Southern Hemisphere during the Mi-1 deglaciation.

Acknowledgements

475 The drilling operations and analyses were funded by the Marsden Fund of the Royal Society of New
Zealand (Grant 11-UOO-043). BRSF was funded by a University of Otago postgraduate
scholarship. Geochemical work was funded by NSF-EAR13-49659 and a Vetlesen Foundation
grant to WJD. The Center for Climate and Life of Columbia University provided funding for
technician support. Thanks are due to Webster Drilling Ltd., the Gibsons, the Macraes, Uwe
480 Kaulfuss, Andy Clifford, and Daniel Jones. We are grateful to the Editor and two anonymous
reviewers for their comments, which significantly improved the final version of this paper.

References

- Adams, C.J., Robinson, P., 1993, Potassium–argon age studies of metamorphism/uplift/cooling in
485 Haast Schist coastal sections south of Dunedin, Otago, New Zealand: *New Zealand Journal
of Geology and Geophysics*, v. 36, p. 317–325.
- Ashkenazy, Y., Gildor, H., 2008, Timing and significance of maximum and minimum equatorial
insolation: *Paleoceanography*, v. 23, PA1206, doi:10.1029/2007PA001436.
- Balsam, W. L., Deaton, B. C., and Damuth, J. E., 1999, Evaluating optical lightness as a proxy for
490 carbonate content in marine sediment cores: *Marine Geology*, v. 161, p. 141–153.
- Bannister, J.M., Lee, D.E., Raine, J.I., 2005, Morphology and paleoenvironmental context of
Fouldenia staminosa, a fossil flower with associated pollen from the Early Miocene of
Otago, New Zealand: *New Zealand Journal of Botany*, v. 43, p. 515–525.
- Bannister, J. M., Conran, J. G., and Lee, D. E., 2012, Lauraceae from rainforest surrounding an

- 495 early Miocene maar lake, Otago, southern New Zealand: Review of Paleobotany and
Palynology, v. 178, p. 13–34.
- Beddow, H.M., Liebrand, D., Sluijs, A., Wade, B.S. and Lourens, L.J., 2016, Global change across
the Oligocene-Miocene transition: High-resolution stable isotope records from IODP Site
U1334 (equatorial Pacific Ocean): *Paleoceanography*, v. 31(1), p. 81–97.
- 500 Berger, A., and Loutre, M. F., 1997, Intertropical latitudes and precessional and half-precessional
cycles: *Science*, v. 278, p. 1476–1478.
- Berger, A., Loutre, M. F., and Mélice, J. L., 2006, Equatorial insolation: from precession harmonics
to eccentricity frequencies: *Climate of the Past*, v. 2, p. 131–136.
- Billups, K., Pälike, H., Channell, J.E.T., Zachos, J.C. and Shackleton, N.J., 2004, Astronomic
505 calibration of the late Oligocene through early Miocene geomagnetic polarity time scale:
Earth and Planetary Science Letters, v. 224(1), p.33–44.
- Cai, W., 2006, Antarctic ozone depletion causes an intensification of the Southern Ocean super-
gyre circulation: *Geophysical Research Letters*, v. 33(3), L03712.
- Chu, G., Liu, J., Sun, Q., Lu, H., Gu, Z., Wang, W., and Liu, T., 2002, The “Mediaeval Warm
510 Period” drought recorded in Lake Huguangyan, tropical South China: *The Holocene*, v. 12,
p. 511–516.
- Chu, G., Liu, J., Schettler, G., Li, J., Sun, Q., Gu, Z., Lu, H., Liu, Q., and Liu, T., 2005, Sediment
fluxes and varve formation in Sihailongwan, a maar lake from northeastern China: *Journal
of Paleolimnology*, v. 34, p. 311–324.
- 515 De Boer, B., Van de Wal, R.S.W., Bintanja, R., Lourens, L.J. and Tuenter, E., 2010, Cenozoic
global ice-volume and temperature simulations with 1-D ice-sheet models forced by benthic
 $\delta^{18}\text{O}$ records: *Annals of Glaciology*, v. 51(55), p. 23–33.
- Debret, M., Desmet, M., Balsam, W., Copard, Y., Francus, P., and Laj, C., 2006,
Spectrophotometer analysis of Holocene sediments from an anoxic fjord: Saanish Inlet,
520 British Columbia, Canada: *Marine Geology*, v. 229, p. 15–28.

- Delmotte, M., Chappellaz, J., Brook, E., Yiou, P., Barnola, J. M., Goujon, C., Raynaud, D., and Lipenkov, V. I., 2004, Atmospheric methane during the last four glacial-interglacial cycles: rapid changes and their link with Antarctic temperature: *Journal of Geophysical Research*, v. 109, D12104, doi: 10.1029/2003JD004417.
- 525 Dettinger, M.D., Ghil, M., Strong, C.M., Weibel, W., Yiou, P., 1995, Software expedites singular-spectrum analysis of noisy time series: *Eos*, v. 76, p. 12, 14, 21.
- Feretti, P., Crowhurst, S.J., Naarfs, B.D.A., and Barbante, C., 2015, The Marine Isotope Stage 19 in the mid-latitude North Atlantic Ocean: astronomical signature and intra-interglacial variability: *Quaternary Science Reviews*, v. 108, p. 95–110.
- 530 Forsyth, P.J., 2001, *Geology of the Waitaki area*. Institute of Geological and Nuclear Sciences 1:250,000 geological map 19. Lower Hutt, New Zealand, Institute of Geological and Nuclear Sciences, 64 p.
- Fox, B. R. S., Wartho, J., Wilson, G. S., Lee, D. E., Nelson, F. E., and Kaulfuss, U., 2015, Long-term evolution of an Oligocene/Miocene maar lake from Otago, New Zealand: *Geochemistry, Geophysics, Geosystems*, v. 16, p. 59–76, doi: 10.1002/2014GC005534.
- 535 Fox, B. R. S., Wilson, G. S., and Lee, D. E., 2016, A unique annually laminated maar lake sediment record shows orbital control of Southern Hemisphere midlatitude climate across the Oligocene-Miocene boundary: *Geological Society of America Bulletin*, March 2016, v. 128, p. 609–626.
- 540 Geotek Ltd., 2014, *Multi-Sensor Core Logger Manual*. Available from <http://www.geotek.co.uk/sites/default/files/MSCLmanual.pdf>.
- Gomez, B., Carter, L., Orpin, A.R., Cobb, K.M., Page, M.J., Trustrum, N.A. and Palmer, A.S., 2012, ENSO/SAM interactions during the middle and late Holocene: *The Holocene*, v. 22(1), p. 23–30.
- 545 Graham, I.J., Mortimer, N., 1992, Terrane characterisation and timing of metamorphism in the Otago Schist, New Zealand, using Rb–Sr and K–Ar geochronology: *New Zealand Journal of*

Geology and Geophysics, v. 35, p. 391–401.

- Ghil, M., Allen, M.R., Dettinger, M.D., Ide, K., Kondrashov, D., Mann, M.E., Robertson, A.W.,
Saunders, A., Tian, Y., Varadi, F., Yiou, P., 2002, Advanced spectral methods for climatic
550 time series: *Reviews of Geophysics*, v. 40, p. 1–41.
- Hagelberg, T. K., Bond, G., and deMenocal, P., 1994, Milankovitch band forcing of sub-
Milankovitch climate variability during the Pleistocene: *Paleoceanography*, v. 9, p. 545–558.
- Hill, K.L., Rintoul, S.R., Coleman, R. and Ridgway, K.R., 2008, Wind forced low frequency
variability of the East Australia Current: *Geophysical Research Letters*, v. 35(8), L08602.
- 555 Kaulfuss, U., Harris, A.C., Conran, J. G., and Lee, D. E., 2014, An early Miocene ant (subfam.
Ambyloponinae) from Foulden Maar: the first fossil Hymenoptera from New Zealand:
Alcheringa, v. 38, p. 568–574, doi: 10.1080/03115518.2014.928181.
- Kushner, P.J., Held, I.M. and Delworth, T.L., 2001, Southern Hemisphere atmospheric circulation
response to global warming: *Journal of Climate*, v. 14(10), p. 2238–2249.
- 560 Lalonde, K., Mucci, A., de Ouellet, A., and Gélinas, Y., 2012, Preservation of organic matter in
sediments promoted by iron: *Nature*, v. 483, p. 198–200.
- Lear, C.H., Rosenthal, Y., Coxall, H.K. and Wilson, P.A., 2004, Late Eocene to early Miocene ice
sheet dynamics and the global carbon cycle: *Paleoceanography*, v. 19(4), PA4015.
- Liebrand, D., Lourens, L.J., Hodell, D.A., De Boer, B., Van de Wal, R.S.W. and Pälike, H., 2011,
565 Antarctic ice sheet and oceanographic response to eccentricity forcing during the early
Miocene: *Climate of the Past*, v. 7(3), p. 869–880.
- Liebrand, D., Beddow, H.M., Lourens, L.J., Pälike, H., Raffi, I., Bohaty, S.M., Hilgen, F.J., Saes,
M.J., Wilson, P.A., van Dijk, A.E. and Hodell, D.A., 2016, Cyclostratigraphy and eccentricity
tuning of the early Oligocene through early Miocene (30.1–17.1 Ma): *Cibicides mundulus*
570 stable oxygen and carbon isotope records from Walvis Ridge Site 1264: *Earth and Planetary*
Science Letters, v. 450, p. 392–405.
- Lindqvist, J.K., Lee, D.E., 2009, High-frequency paleoclimate signals from Foulden Maar,

Waipiata Volcanic Field, southern New Zealand: An Early Miocene varved lacustrine diatomite deposit: *Sedimentary Geology*, v. 222, p. 98–110.

575 Lu, H. Y., Liu, J. Q., Chu, G.-Q., Gu, Z.-Y., Negendank, J., Schettler, G., and Mingram, J., 2003, A study of pollen and environment in the Huguangyan maar lake since the last glaciation: *Acta Palaeontologica Sinica*, v. 42, p. 284–291.

Mawbey, E.M. and Lear, C.H., 2013, Carbon cycle feedbacks during the Oligocene-Miocene transient glaciation: *Geology*, v. 41, p. 963–966.

580 Mayewski, P. A., Meeker, L. D., Twickler, M. S., Whitlow, S., Yang, Q., Lyons, W. B., and Prentice, M., 1997, Major features and forcing of high-latitude northern hemisphere atmospheric circulation using a 100,000-year long glaciochemical series: *Journal of Geophysical Research*, v. 102, p. 26,345–26,366.

Miller, K.G., Wright, J.D., Fairbanks, R.G., 1991, Unlocking the ice house—Oligocene–Miocene
585 oxygen isotopes, eustasy, and margin erosion: *Journal of Geophysical Research*, v. 96, p. 6829–6848.

Mingram, J., Schettler, G., Nowaczyk, N., Luo, X., Lu, H., Liu, J. and Negendank, J.F., 2004, The Huguang maar lake—a high-resolution record of palaeoenvironmental and palaeoclimatic changes over the last 78,000 years from South China: *Quaternary International*, v. 122(1), p.
590 85–107.

Morel, F. M. M., and Hudson, R. J. M., 1985, The geobiological cycle of trace elements in aquatic systems: Redfield revisited: in Stumm, W., ed., *Chemical Processes in Lakes*: New York, John Wiley and Sons, p. 251–282.

Moreno, P. I., Francois, J. P., Villa-Martínz, R. P., and Moy, C. M., 2004, Millennial-scale
595 variability in Southern Hemisphere westerly wind activity over the last 5000 years in SW Patagonia: *Quaternary Science Reviews*, v. 28, p. 25–38.

Moreno, P. I., Francois, J. P., Moy, C. M., and Villa-Martínez, R., 2010, Covariability of the Southern Westerlies and atmospheric CO₂ during the Holocene: *Geology*, v. 38, p. 727–730.

- Muramoto, J. A., Hono, S., Fry, B., Hay, B. J., Howarth, R. W., and Cisne, J. L., 1991, Sulfur, iron
600 and organic carbon fluxes in the Black Sea: sulfur isotopic evidence for origin of sulfur
fluxes: *Deep-Sea Research*, v. 38, p. S1151–S1187.
- Pälike, H., Frazier, J. and Zachos, J.C., 2006a, Extended orbitally forced palaeoclimatic records
from the equatorial Atlantic Ceara Rise: *Quaternary Science Reviews*, v. 25(23), p. 3138–
3149.
- 605 Pälike, H., Norris, R.D., Herrle, J.O., Wilson, P.A., Coxall, H.K., Lear, C.H., Shackleton, N.J.,
Tripathi, A.K. and Wade, B.S., 2006b, The heartbeat of the Oligocene climate system.
Science, v. 314(5807), p. 1894–1898.
- Paul, H.A., Zachos, J.C., Flower, B.P. and Tripathi, A., 2000, Orbitally induced climate and
geochemical variability across the Oligocene/Miocene boundary: *Paleoceanography*, v.
610 15(5), p.471–485.
- Pokras, E. M., and Mix, A. C., 1987, Earth's precession cycle and Quaternary climatic change in
tropical Africa: *Nature*, v. 326, p. 486–487.
- Reichgelt, T., Kennedy, E. M., Mildenhall, D. C., Conran, J. G., Greenwood, D. R. and Lee, D. E.,
2013, Quantitative paleoclimate estimates for Early Miocene southern New Zealand:
615 Evidence from Foulden Maar: *Palaeogeography, Palaeoclimatology, Palaeoecology*, v. 378, p.
36–44.
- Reichgelt, T., D'Andrea, W.J., and Fox, B.R.S., 2016, Abrupt plant physiological changes in
southern New Zealand at the termination of the Mi-1 event reflect shifts in hydroclimate and
 $p\text{CO}_2$: *Earth and Planetary Science Letters*, v. 455, p. 115–124.
- 620 Renssen, H., Goosse, H., Fichefet, T., Masson-Delmotte, V. and Koç, N., 2005, Holocene climate
evolution in the high-latitude Southern Hemisphere simulated by a coupled atmosphere-sea
ice-ocean-vegetation model: *The Holocene*, v. 15(7), p. 951–964.
- Roemmich, D., Gilson, J., Davis, R., Sutton, P., Wijffels, S. and Riser, S., 2007, Decadal spinup of
the South Pacific subtropical gyre: *Journal of Physical Oceanography*, v. 37(2), p.162–173.

- 625 Round, F. E., Crawford, R. M., and Mann, D. G., 1990, *The Diatoms: Biology and Morphology of the Genera*: Cambridge, Cambridge University Press, 747 pp.
- Schettler, G., Liu, Q., Mingram, J., Stebich, M. and Dulski, P., 2006, East-Asian monsoon variability between 15 000 and 2000 cal. yr BP recorded in varved sediments of Lake Sihailongwan (northeastern China, Long Gang volcanic field): *The Holocene*, v. 16(8), p. 1043–1057.
- 630 Schneider, R. R., Cramp, A., Damuth, J. E., Hiscott, R. N., Kowsmann, R. O., Lopez, M., Nanayama, F., Normark, W. R., and Shipboard Scientific Party, 1995, Color-reflectance measurements obtained from Leg 155 cores: in Flood, R. D., Piper, D. J. W., Klaus, A. et al., eds., *Proceedings of the Ocean Drilling Program, Initial Reports*, v. 155, p. 697–700.
- 635 Short, D. A., Mengel, J. G., Crowley, T. J., Hyde, W. T., and North, G. R., 1991, Filtering of Milankovitch cycles by Earth's geography: *Quaternary Research*, v. 35, p. 157–173.
- Shulmeister, J., Goodwin, I., Renwick, J., Harle, K., Armand, L., McGlone, M.S., Cook, E., Dodson, J., Hesse, P.P., Mayewski, P. and Curran, M., 2004, The Southern Hemisphere westerlies in the Australasian sector over the last glacial cycle: a synthesis: *Quaternary International*, v. 118, p. 23–53.
- 640 Stewart, R.B. and Neall, V.E., 1984, Chronology of palaeoclimatic change at the end of the last glaciation: *Nature*, v. 311, p. 47–48.
- Striewski, B., Mayr, C., Flenley, J., Naumann, R., Turner, G., and Lücke, A., 2009, Multi-proxy evidence of late Holocene human-induced environmental changes at Lake Pupuke, Auckland (New Zealand): *Quaternary International*, v. 202, p. 69–93.
- 645 Striewski, B., Shulmeister, J., Augustinus, P. C., and Soderholm, J., 2013, Late Holocene climate variability from Lake Pupuke maar, Auckland, New Zealand: *Quaternary Science Reviews*, v. 77, p. 46–54.
- Torrence, C., and Compo, G. P., 1998, A practical guide to wavelet analysis: *Bulletin of the American Meteorological Society*, v. 79, p. 61–78.
- 650

- Venables, W.N., and Ripley, B.D., 2002, *Modern Applied Statistics with S*: Berlin: Springer.
- Wang, L., Rioual, P., Panizzo, V. N., Lu, H., Gu, Z., Chu, G., Yang, D., Han, J., and Mackay, A.,
2012, A 1000-yr record of environmental change in NE China indicated by diatom
assemblages from maar lake Erlongwan: *Quaternary Research*, v. 78, p. 24–34.
- 655 Wilson, G. S., Pekar, S. F., Naish, T. R., Passchier, S., and DeConto, R., 2008, The Oligocene–
Miocene Boundary–Antarctic Climate Response to Orbital Forcing. In: Florindo, F., and
Siegert, M., *Antarctic Climate Evolution, Developments in Earth and Environmental Sciences*
8, p. 369–400.
- Yiou, P., Jouzel, J., Johnsen, S., and Rögnvaldsson, Ö. E., 1995, Rapid oscillations in Vostok and
660 GRIP ice cores: *Geophysical Research Letters*, v. 22, p. 2179–2182.

Figure Captions

Figure 1: Geographical and geological context of Foulden Maar, modified from Fox et al. (2016).

665 (a) Otago and Southland, showing location of Foulden Maar. Inset shows location in New Zealand.
(b) Plate tectonic reconstruction of the New Zealand region in the early Miocene, after Cande and Stock (2004). Dashed lines show modern-day bathymetric contours at 1000 m intervals. Dotted red line shows long-term average position of combined Subantarctic and Subtropical Fronts, as
670 are modern-day land areas. Black dot indicates approximate location of Foulden Maar.

Figure 2: Time series of (a) density, (b) magnetic susceptibility, (c) b^* , (d) L^* and (e) total organic carbon. Parts a-d have both the full dataset with a 10-yr interval (grey line) and the reduced dataset with a ~2000-yr interval (black line).

675

Figure 3: Blackman-Tukey spectra of four physical properties from the Foulden Maar lake sediment deposit. Period is plotted logarithmically to allow clearer visualisation of data, and individual points are shown to indicate resolution in each part of the spectrum. The thin dashed line indicates the AR(1) spectrum. Significant peaks are annotated with period (in kyr). (a) Density; (b) magnetic
680 susceptibility; (c) b^* (blue-yellow hue); (d) L^* (brightness).

Figure 4: a-d bandpass-filtered physical properties. Bandpass filtering was performed using a butterworth filter with critical frequencies of 1/5,000 years and 1/15,000 years. e, maximum insolation at the Equator for the period of deposition at Foulden Maar (calculated using the orbital
685 solution presented in Laskar et al., 2004).

Figure 5: Wavelet spectra of four physical properties from the Foulden Maar sediment. Region

where power rises above 95% significance is enclosed in a solid black line. Periods of significant cycles detected by Blackman-Tukey analysis (see Figure 2) are indicated by dashed lines. (a) 690 Density; (b) magnetic susceptibility; (c) b^* ; (d) L^* .

Figure 6: Principal component analysis of the full dataset (a-b) and the resampled dataset (c-d). (a) and (c) show the first principal component (PC1) on the x-axis and PC2 on the y-axis. (b) and (d) show PC1 on the x-axis and PC3 on the y-axis. In both the full and resampled dataset, the first three 695 principal components explain ~90% of the variance.

Figure 7: Reconstructed principal component timeseries. (a) PC1, full dataset; (b) PC2, full dataset; (c) PC3, full dataset; (d) PC1, resampled dataset; (e) PC2, resampled dataset; (f) PC3, resampled dataset. Comparisons between reconstructed principal components and physical properties datasets 700 can be found in the supplementary material.

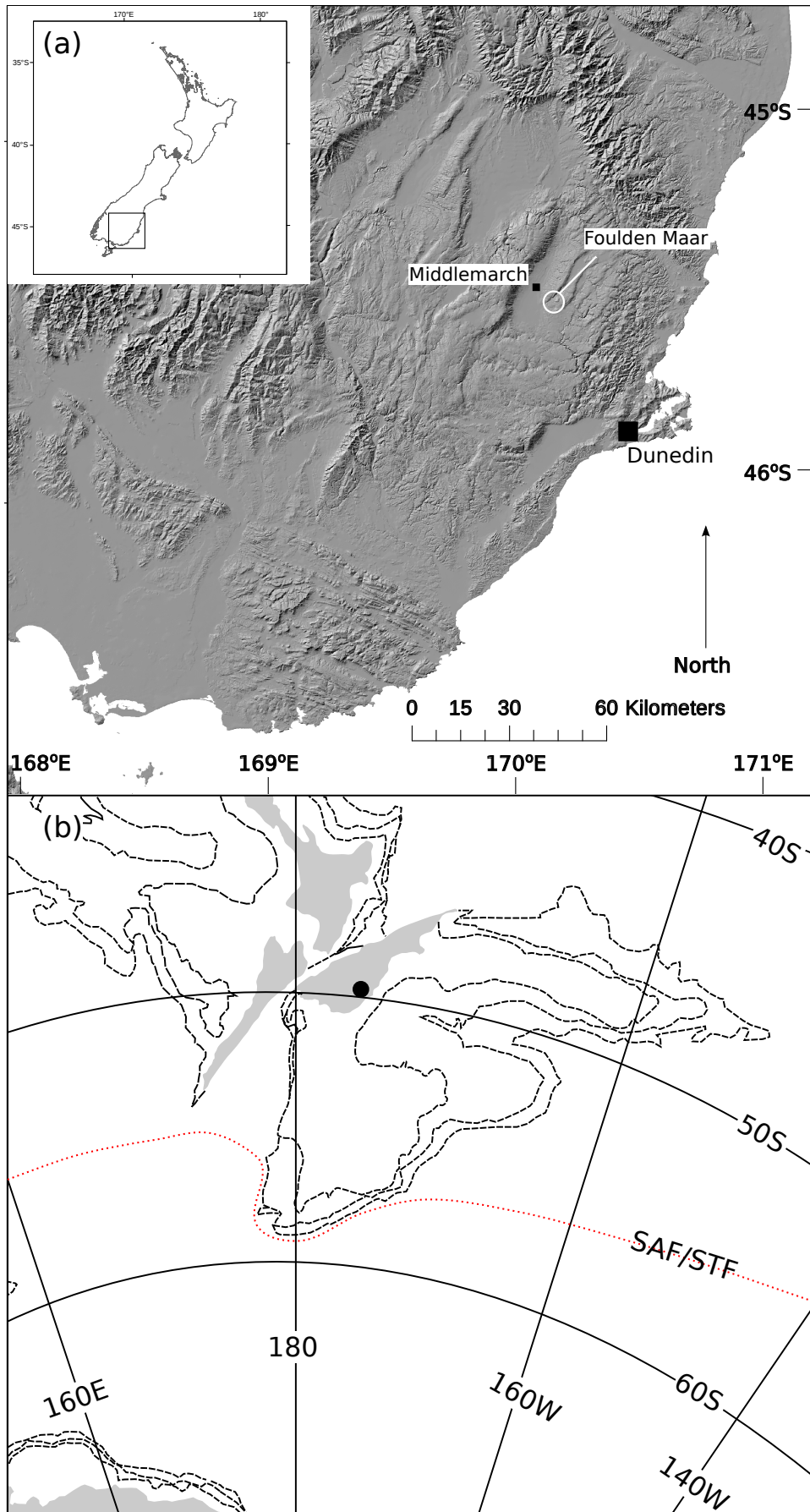
Figure 8: Comparison between the reconstructed first principal components of the full dataset (grey line) and the resampled dataset, including TOC (black line).

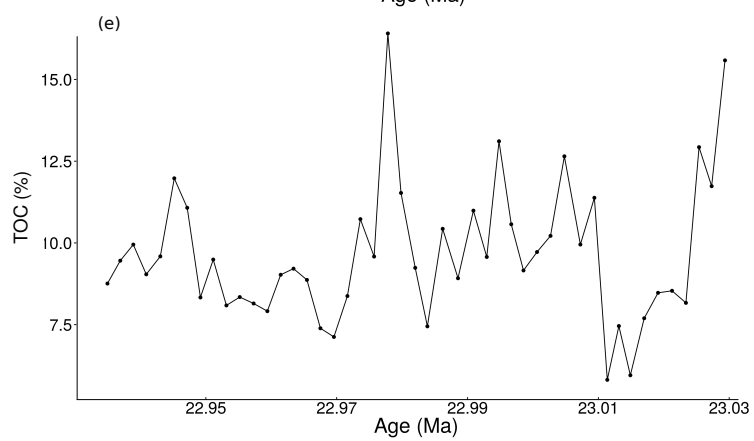
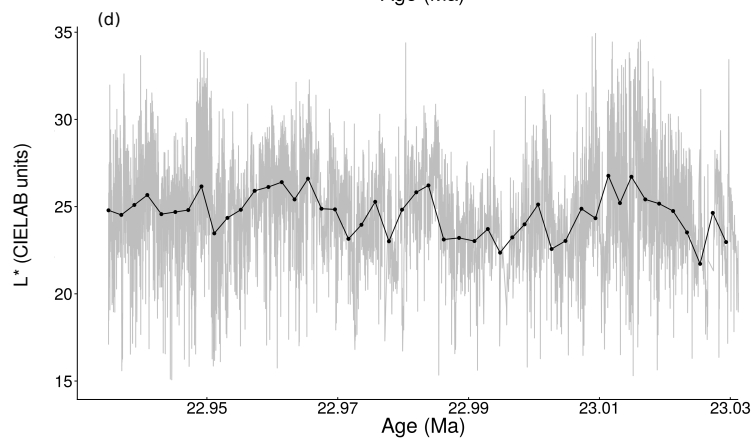
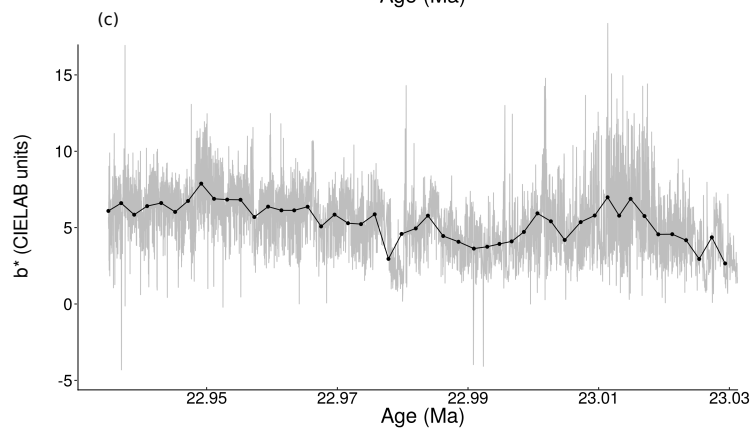
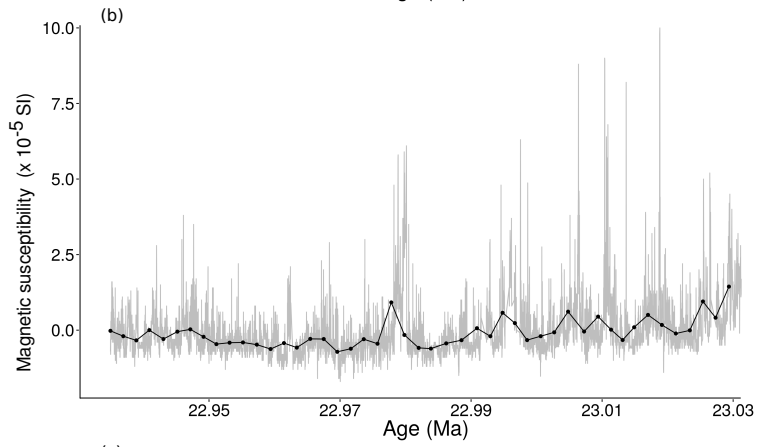
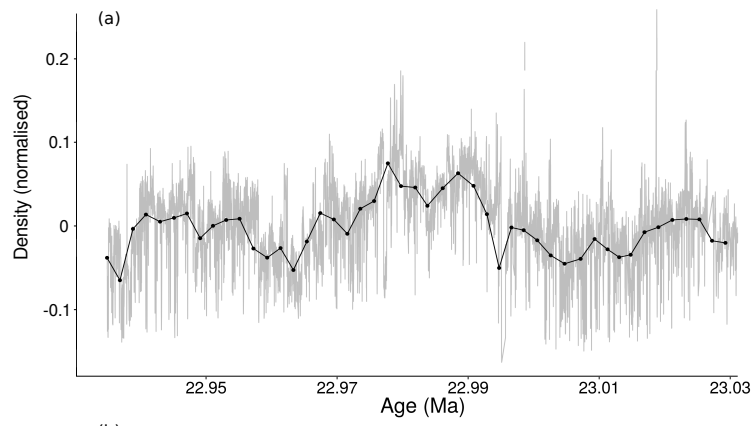
705 Figure 9: Blackman-Tukey analysis of the first three principal components of the full dataset. Period is plotted logarithmically to allow clearer visualisation of data, and individual points are shown to indicate resolution in each part of the spectrum. The thin dashed line indicates the AR(1) spectrum. Significant peaks are annotated with period (in kyr). (a) PC1; (b) PC2; (c) PC3.

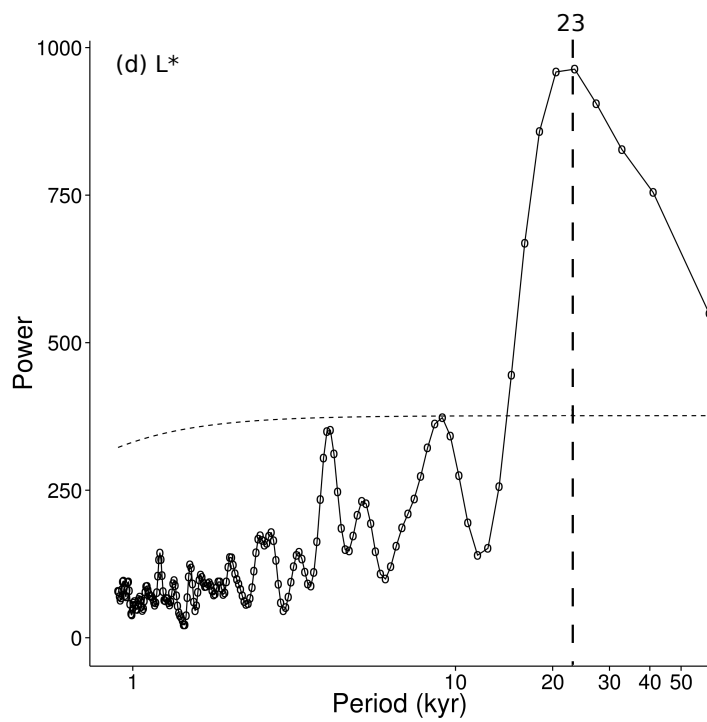
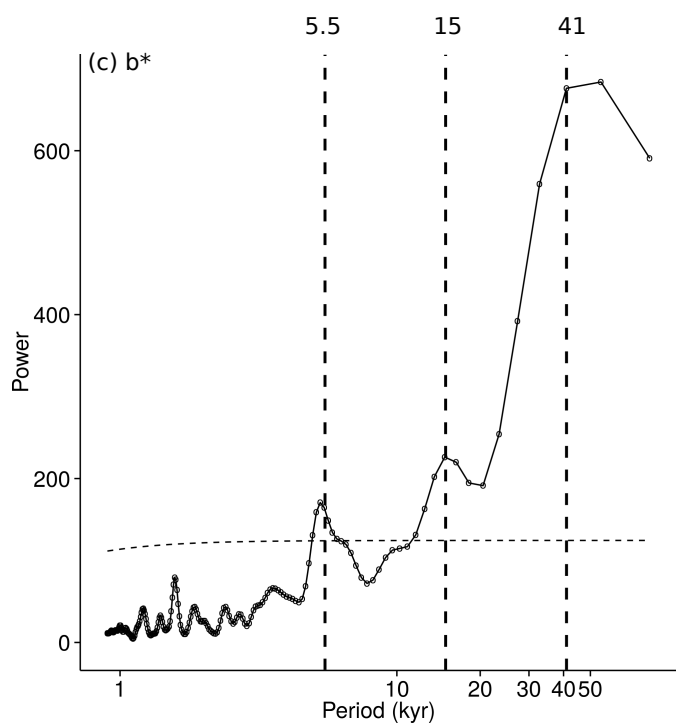
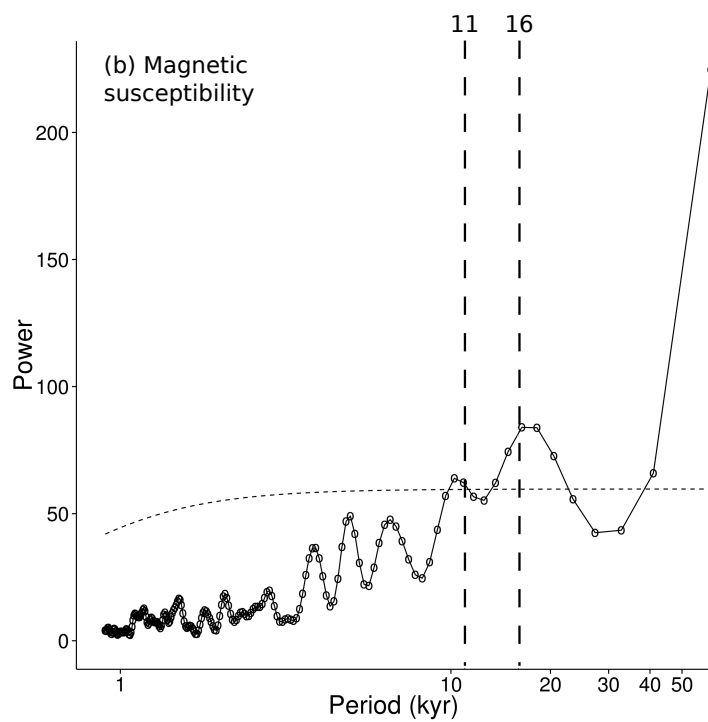
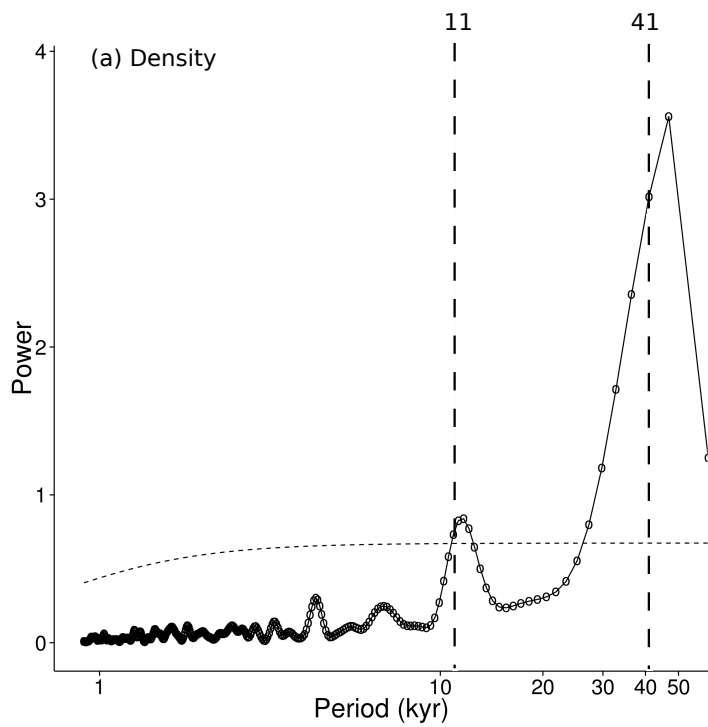
710 Table 1: Component loadings for the five variables for the first three principal components in the full and resampled datasets. Note no values for TOC in the full dataset.

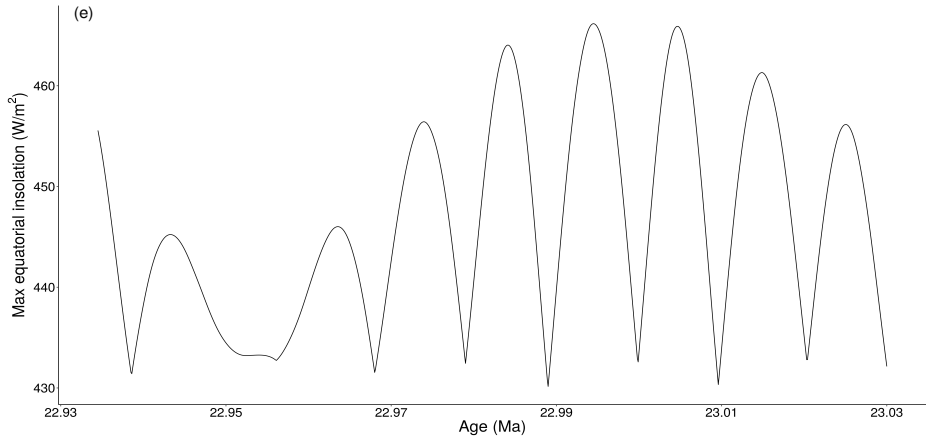
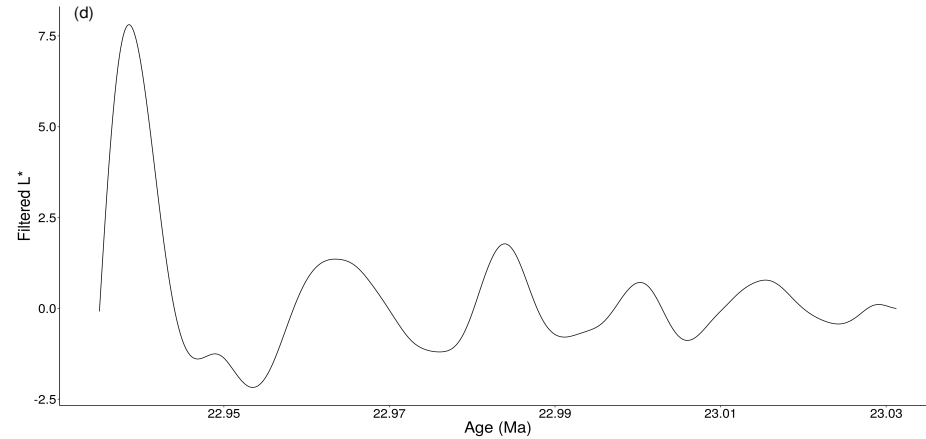
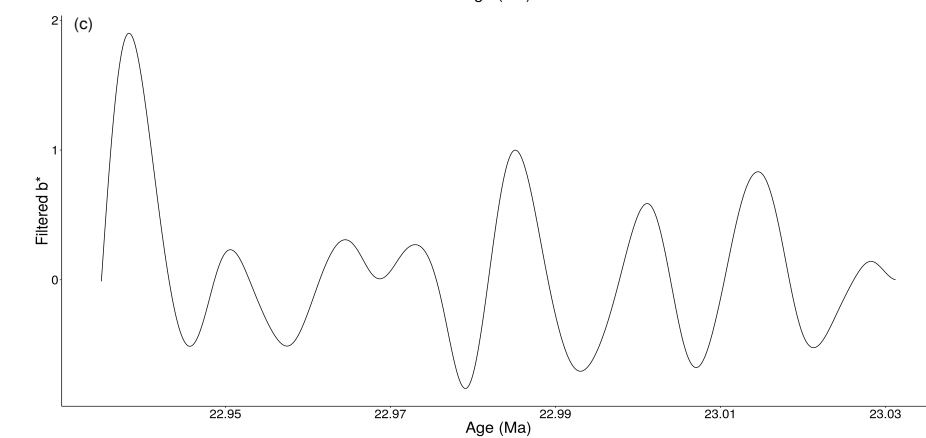
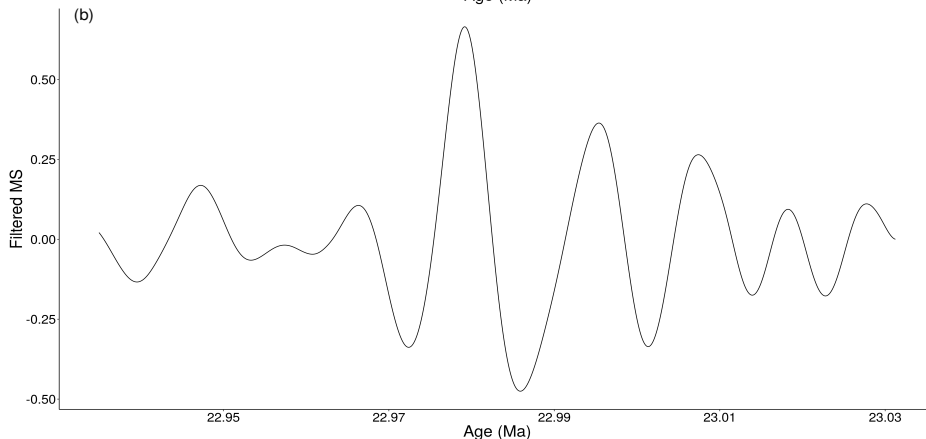
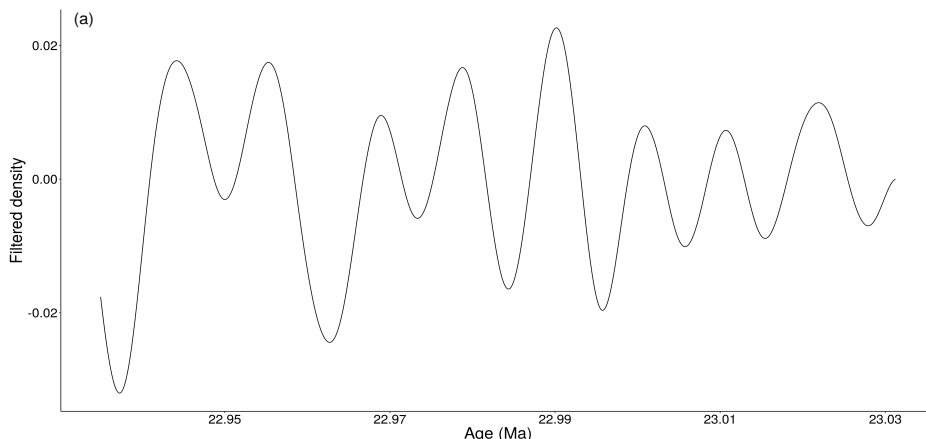
Table 2: Ages of dark laminated diatomite (DLDA) intervals in core FH2, along with the length of

each interval and the length between intervals.

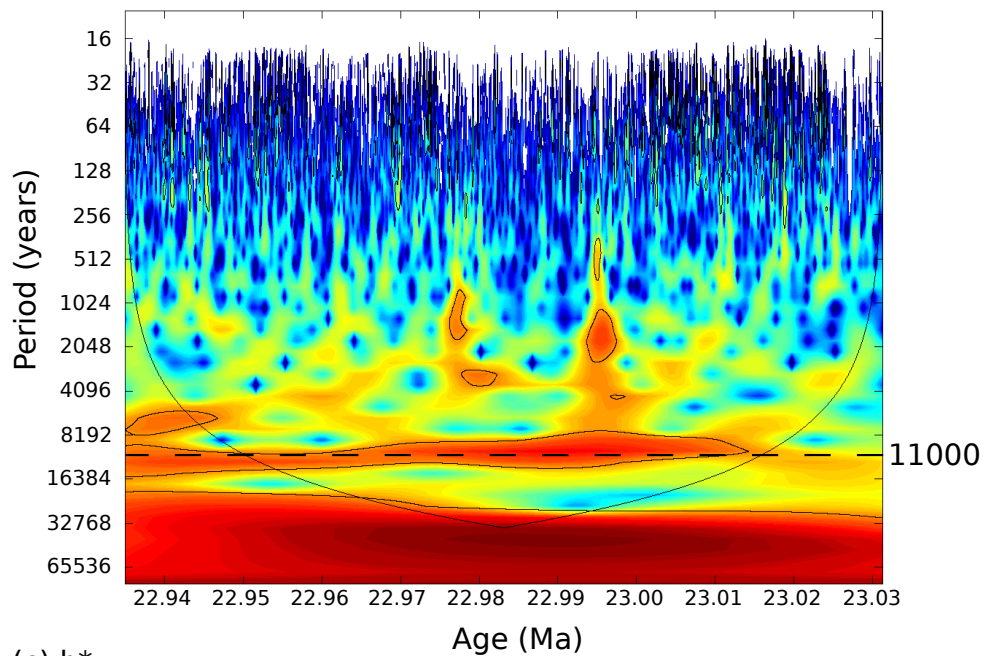




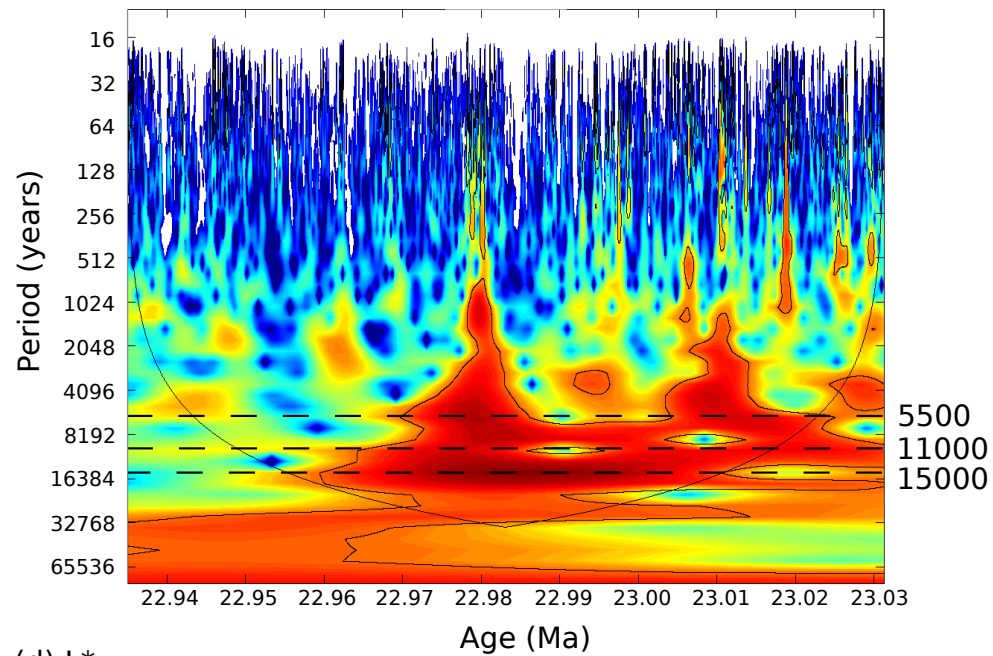




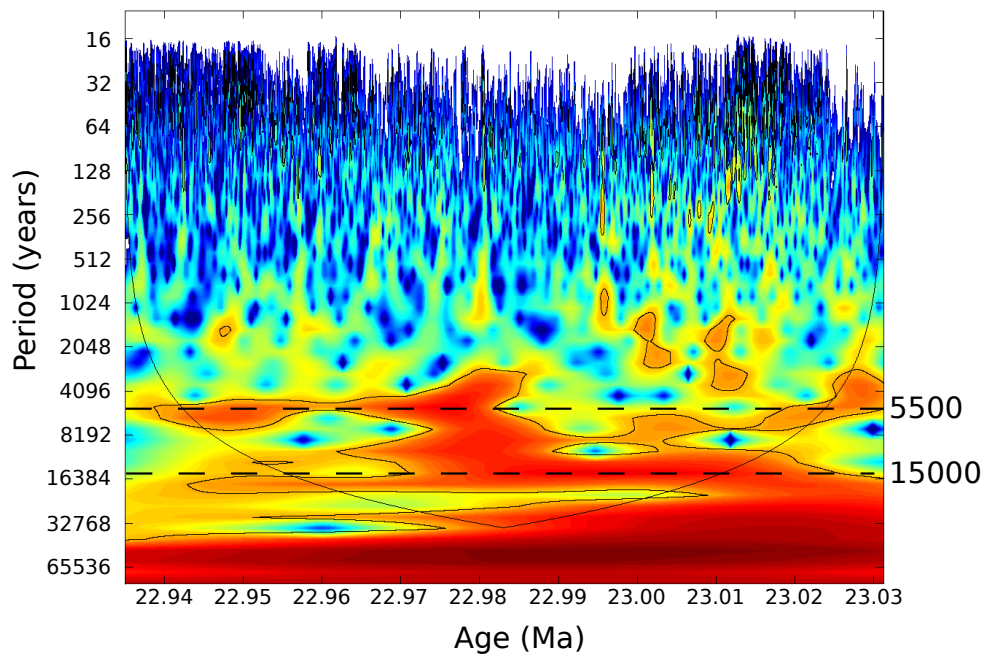
(a) Gamma attenuation density



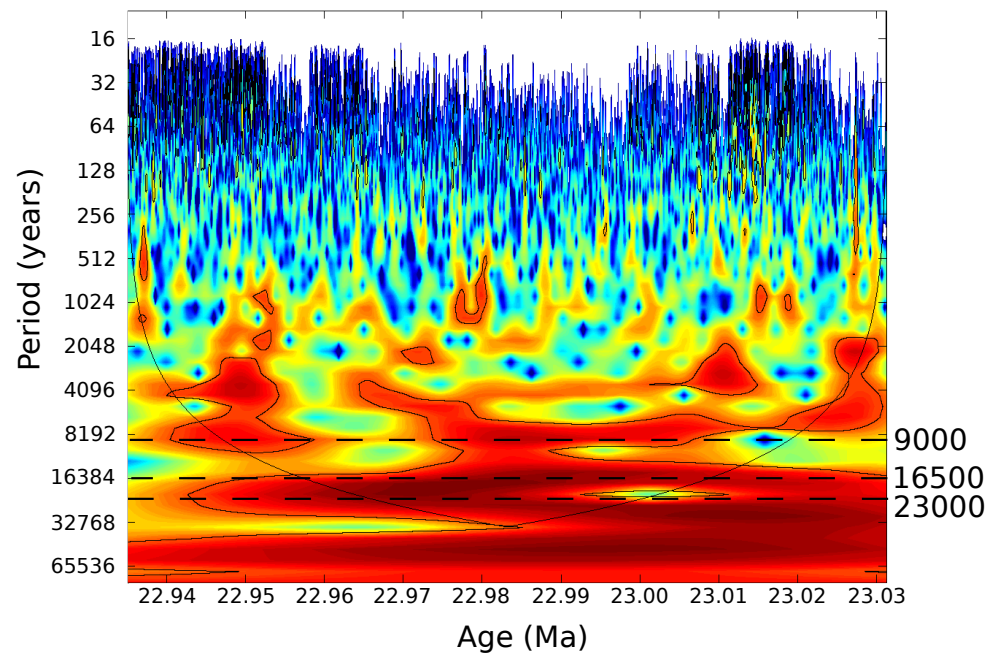
(b) Magnetic susceptibility

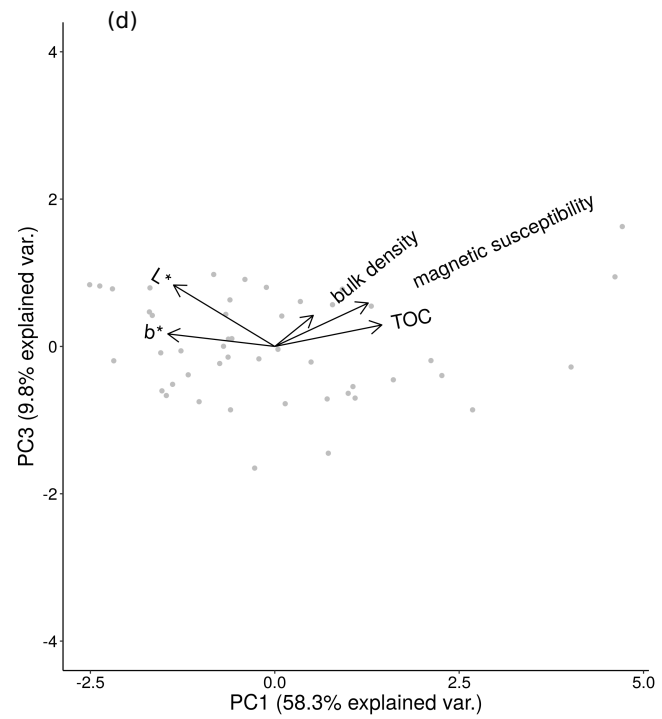
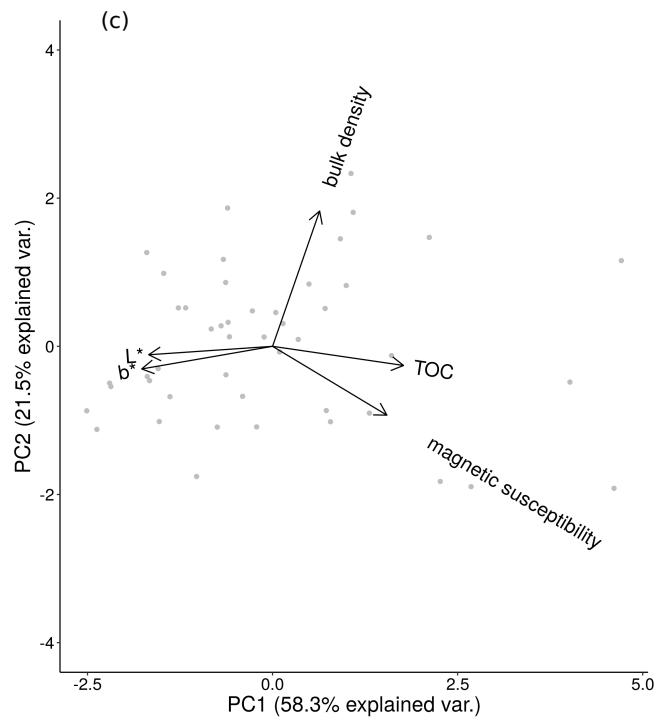
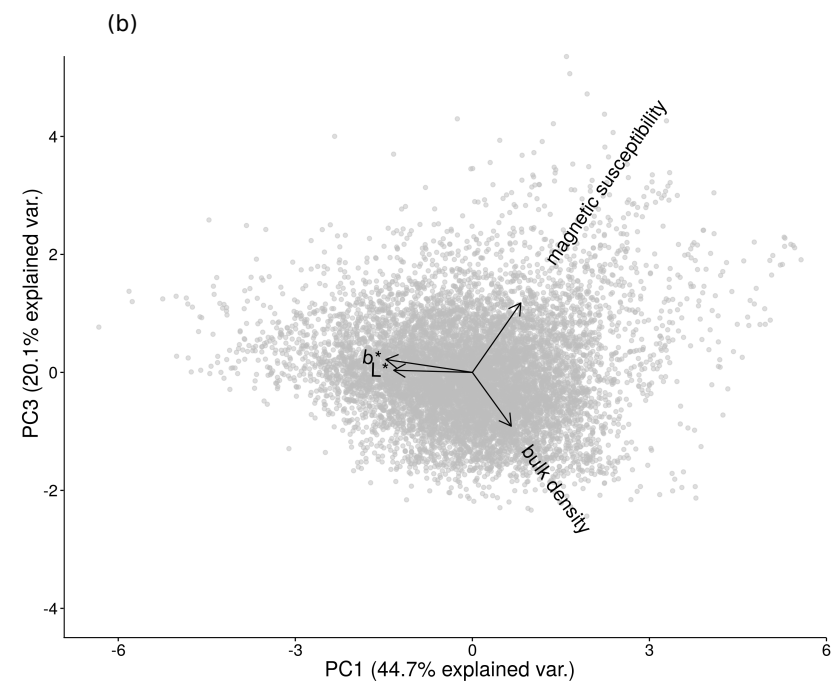
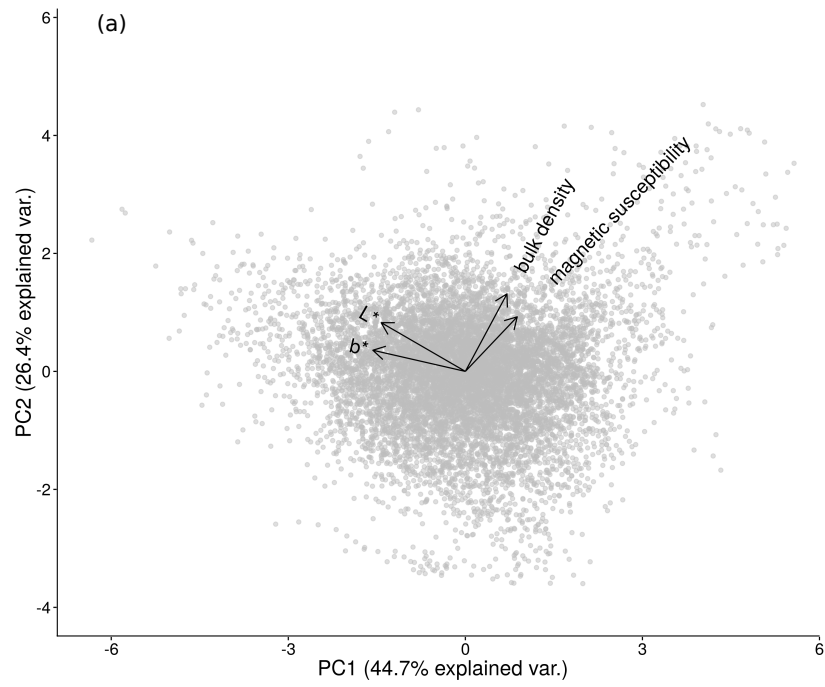


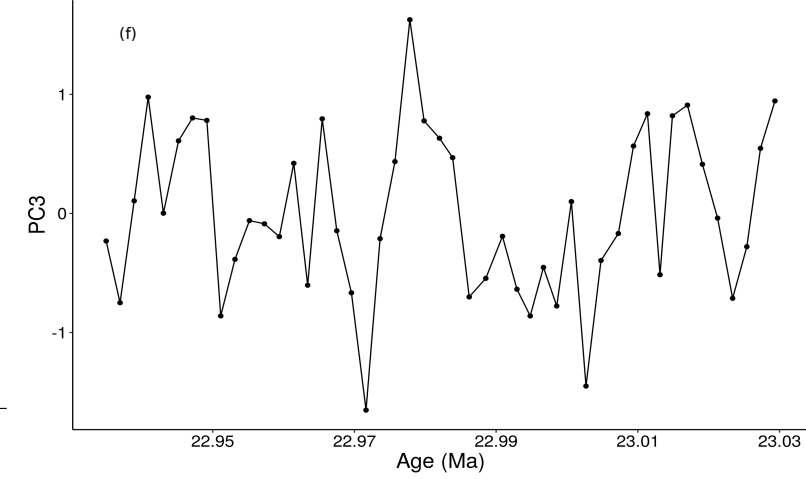
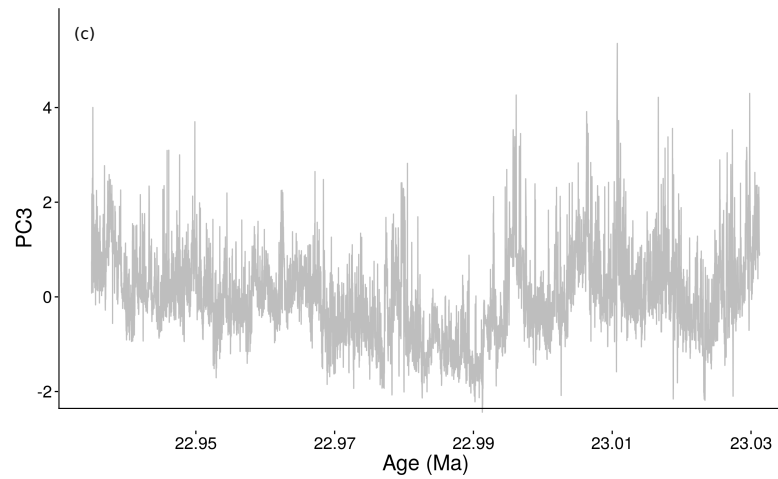
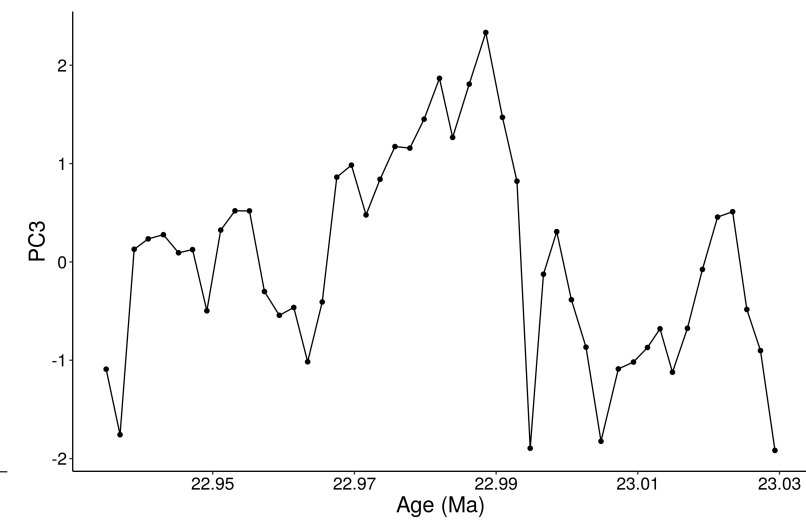
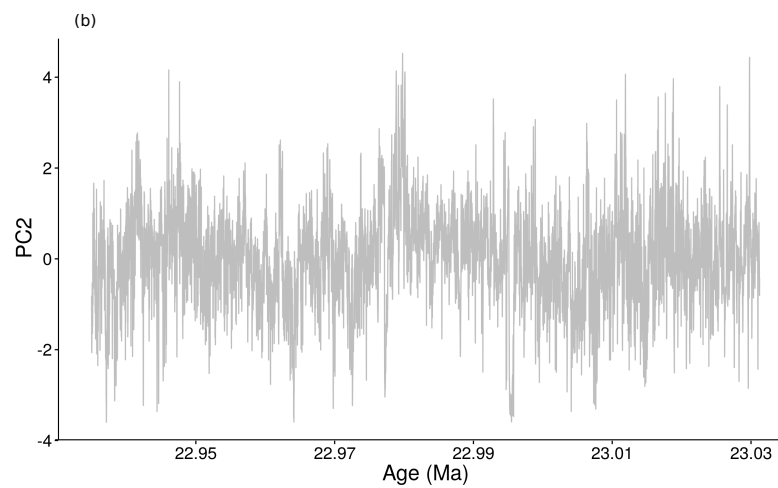
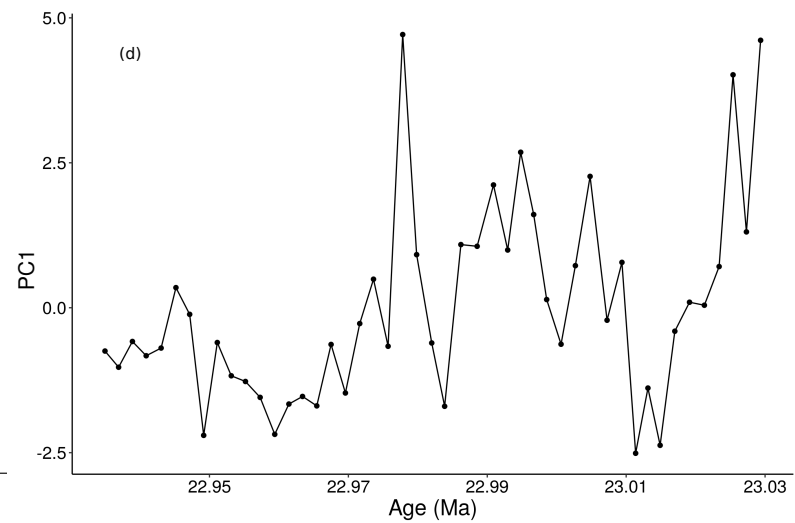
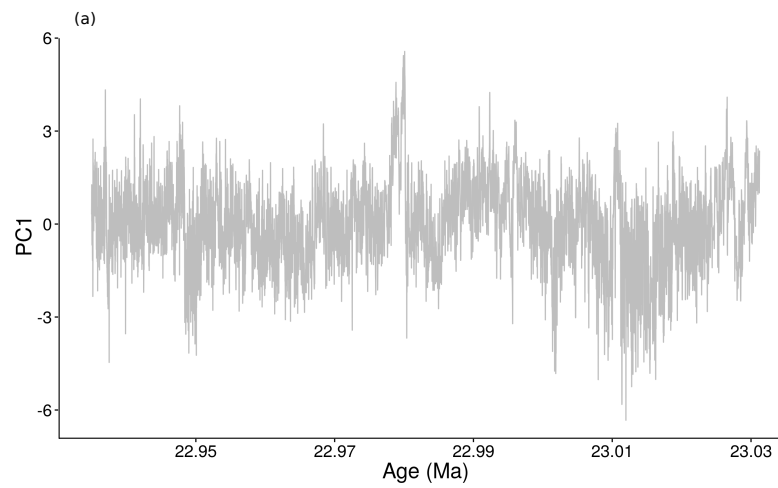
(c) b^*

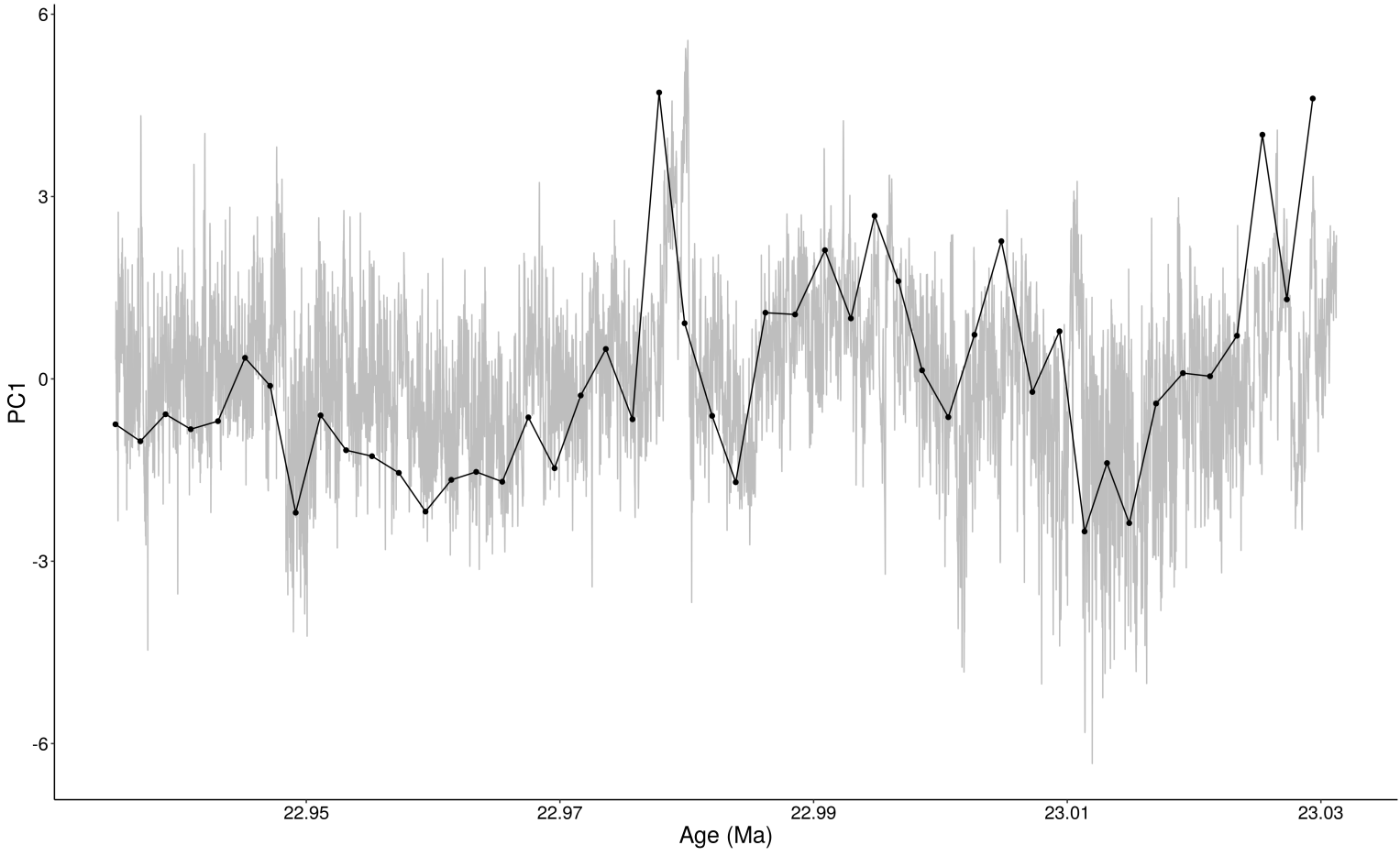


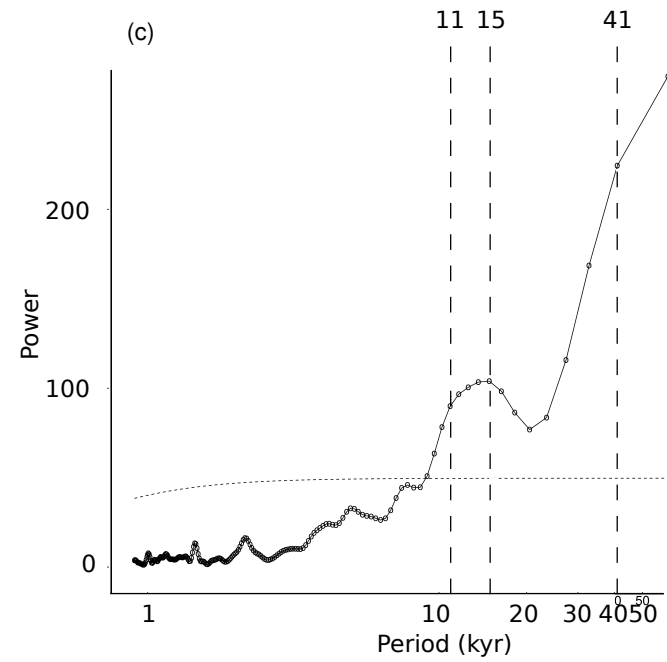
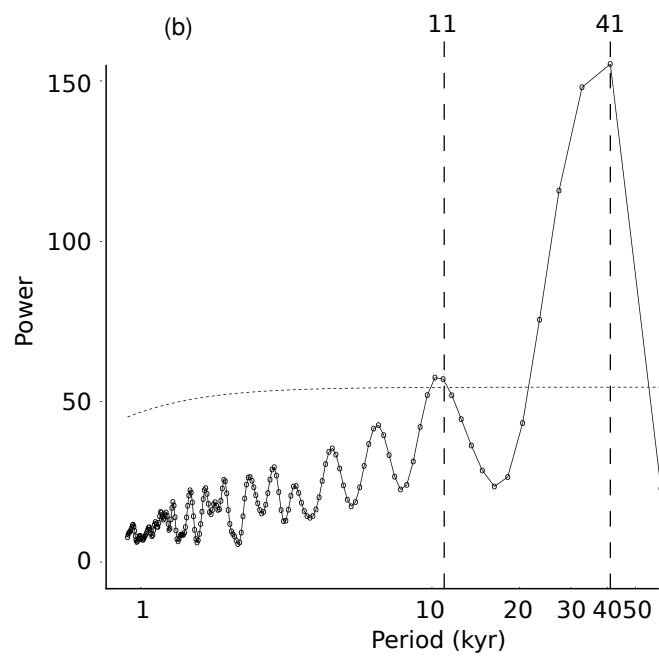
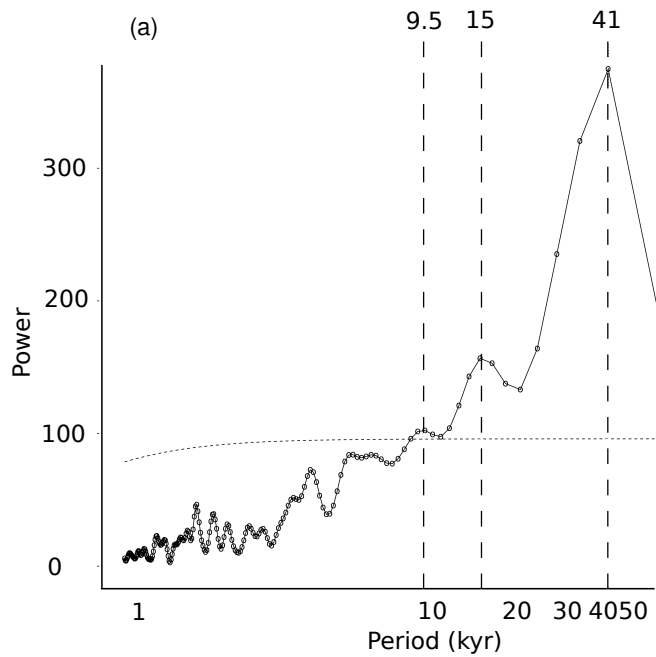
(d) L^*











Sheet1

	Full dataset			Resampled dataset		
	PC1	PC2	PC3	PC1	PC2	PC3
Density	0.29	0.71	-0.61	0.18	0.87	0.36
Magnetic	0.37	0.5	0.78	0.45	-0.44	0.51
L*	-0.59	0.45	0.02	-0.49	-0.05	0.72
b*	-0.65	0.19	0.14	-0.51	-0.15	0.15
TOC	-	-	-	0.51	-0.12	0.25

Sheet1

Interval top age (Ma)	Interval base age (Ma)	Interval central age (Ma)	Interval length (yr)	Inter interval length (yr)
22.978232	22.98017	22.979201	1938.00	NA
22.992237	22.998918	22.9955775	6681.00	16376.50
23.0101	23.011195	23.0106475	1095.00	15070.00
23.024346	23.027436	23.025891	3090.00	15243.50
23.028784	23.03125	23.030017	2466.00	4126.00

Supplementary material for Fox et al., Interaction of polar and tropical influences in the mid-latitudes of the Southern Hemisphere during the Mi-1 deglaciation

1. Details of error propagation undertaken on previously published $^{40}\text{Ar}/^{39}\text{Ar}$ dates from Foulden Maar

There is a magnetic reversal (reversed \rightarrow normal) at the base of the lake sediment interval in core FH2. $^{40}\text{Ar}/^{39}\text{Ar}$ dates reported in Timm et al. (2010) and Fox et al. (2015) were used to constrain the age of this reversal in Fox et al. (2016). The reversal was identified with the base of Chron C6Cn.2n (23.033 Ma, the Oligocene/Miocene boundary; Fox et al., 2016), and this formed the basis of the age model for the Foulden Maar lake sediment. However, the $^{40}\text{Ar}/^{39}\text{Ar}$ dates and errors reported in Timm et al. (2010) and Fox et al. (2015) only quoted internal errors. Following revised best practice for reporting $^{40}\text{Ar}/^{39}\text{Ar}$ ages, we here recalculate the errors associated with these dates.

The $^{40}\text{Ar}/^{39}\text{Ar}$ dating technique is derived from the older K-Ar absolute dating method, in that both utilize the radioactive decay of parent ^{40}K to daughter ^{40}Ar . However, unlike the K-Ar absolute dating method, $^{40}\text{Ar}/^{39}\text{Ar}$ dating is a relative geochronology technique, as it requires the co-determination of unknown samples with pre-determined age standards. Samples and age standards are fast-neutron irradiated in a canister to convert ^{39}K to ^{39}Ar , with ^{39}Ar becoming the proxy-parent isotope for ^{40}K . Therefore, the $^{40}\text{Ar}/^{39}\text{Ar}$ sample age is calculated from the following equation:

$$t = \frac{1}{\lambda} \ln \left(1 + J \frac{^{40}\text{Ar}^*}{^{39}\text{Ar}} \right)$$

Where t is the age of the sample, λ is the total decay constant of ^{40}K , J is the value calculated from the measurement of the co-irradiated age standards, and $^{40}\text{Ar}^*/^{39}\text{Ar}$ is the ratio of radiogenic ^{40}Ar daughter isotope and the proxy-parent $^{39}\text{Ar}_K$ isotope of the sample. The age standards used to determine the J value can be in the form of primary standards (dated via K-Ar methods), or secondary standards (determined from $^{40}\text{Ar}/^{39}\text{Ar}$ studies of multiple secondary standards that also include a primary standard, e.g., Renne et al., 1998, and Schwarz and Trieloff, 2007).

However, the published dates of $^{40}\text{Ar}/^{39}\text{Ar}$ secondary age standards can vary by $\sim 1\%$ (e.g., Kuiper et al., 2008). Therefore, discussions in the $^{40}\text{Ar}/^{39}\text{Ar}$ community have prompted the need to: (1) recalculate $^{40}\text{Ar}/^{39}\text{Ar}$ ages and errors where different primary and/or secondary standard published ages, decay constants, and $^{40}\text{K}/\text{K}$ production ratios are used; and (2) to quote “internal” and “external” errors associated with $^{40}\text{Ar}/^{39}\text{Ar}$ ages (e.g., Renne et al., 1998; Min et al., 2000; Koppers, 2002). Many $^{40}\text{Ar}/^{39}\text{Ar}$ dates in the literature only contain errors associated with the analytical and J value uncertainties from the unknown sample, and are hereby termed “internal errors” (e.g., option ^a in the recalculated ages below). Analytical uncertainties include errors obtained from the measurement of the mass spectrometer detector baselines, argon isotopes in

the sample and blank analyses, mass spectrometer discrimination corrections, the atmospheric $^{40}\text{Ar}/^{36}\text{Ar}$ ratio, and nuclear interference correction factors from Ca-, K-, and Cl-derived isotopes determined from measurements of co-irradiated K and Ca salts.

$^{40}\text{Ar}/^{39}\text{Ar}$ dates that include the “internal errors” of both the sample and secondary standard (e.g., option ^b in the recalculated errors below) are considered to be a minimum absolute error of a sample (Koppers, 2002). “External errors” are hereby defined as errors associated with the ^{40}K decay constants, and the $^{40}\text{K}/\text{K}$ production ratio and error (e.g., Garner et al., 1965) of the age standards. Therefore, the external errors of the secondary age standard plus the internal errors of the sample yield a more robust $^{40}\text{Ar}/^{39}\text{Ar}$ absolute error (e.g., option ^c in the recalculated errors below), and we are utilizing these $^{40}\text{Ar}/^{39}\text{Ar}$ dates and recalculated errors for the purpose of this Foulden Maar study.

The date and error recalculations were undertaken by a series of partial derivatives (e.g., equation 24 in Koppers, 2002) on our three Foulden Maar $^{40}\text{Ar}/^{39}\text{Ar}$ ages of interest, yielding recalculated dates and errors of:

Basalt sample V14 = $23.38 \pm 0.24^{\text{a}} (\pm 0.30)^{\text{b}} [\pm 0.43]^{\text{c}}$ Ma (2σ ; Fox et al., 2015).

Basalt sample V15 = $24.51 \pm 0.24^{\text{a}} (\pm 0.30)^{\text{b}} [\pm 0.45]^{\text{c}}$ Ma (2σ ; Fox et al., 2015).

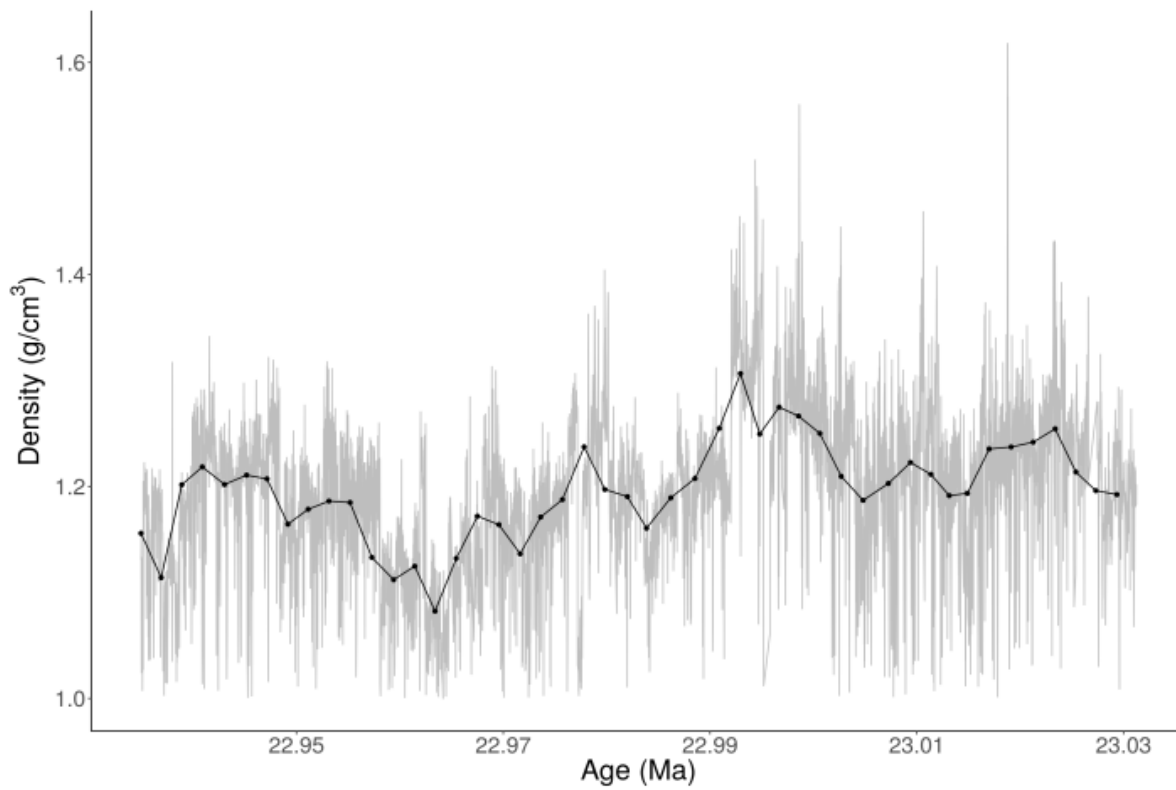
Basalt sample V2A = $23.17 \pm 0.37^{\text{a}} (\pm 0.38)^{\text{b}} [\pm 0.49]^{\text{c}}$ Ma (2σ ; Timm et al., 2010).

The recalculated $^{40}\text{Ar}/^{39}\text{Ar}$ errors incorporate uncertainties associated with: (1) the ^{40}K decay constants of Steiger and Jäger (1977) using the % errors of Beckinsale and Gale (1969), e.g., total ^{40}K decay = $5.543 \pm 0.0098 \times 10^{-10}$ years; 1σ); (2) the $^{40}\text{K}/\text{K}$ abundance ratios of Garner et al. (1975), e.g., $^{40}\text{K} = 0.01167 \pm 0.00004$ (1σ); and, (3) the secondary standard ages and errors of HD-B1 biotite (24.18 ± 0.09 Ma; 1σ internal error; Schwarz and Trieloff, 2007) for samples V14 and V15 from Fox et al. (2015), and TCS sanidine (27.87 ± 0.04 Ma; 1σ internal error; M.A. Lanphere, pers. comm.) for sample V2A from Timm et al. (2010). The dates of the two secondary age standards (HD-B1 biotite and TCS sanidine) used in these two Foulden Maar studies have been independently verified to the same primary age standard (SB-3 biotite; 162.9 ± 0.9 Ma; 1σ internal error) by both Lanphere and Dalrymple (2000) and Schwarz and Trieloff (2007), giving us additional confidence in the recalculated absolute $^{40}\text{Ar}/^{39}\text{Ar}$ dates and errors.

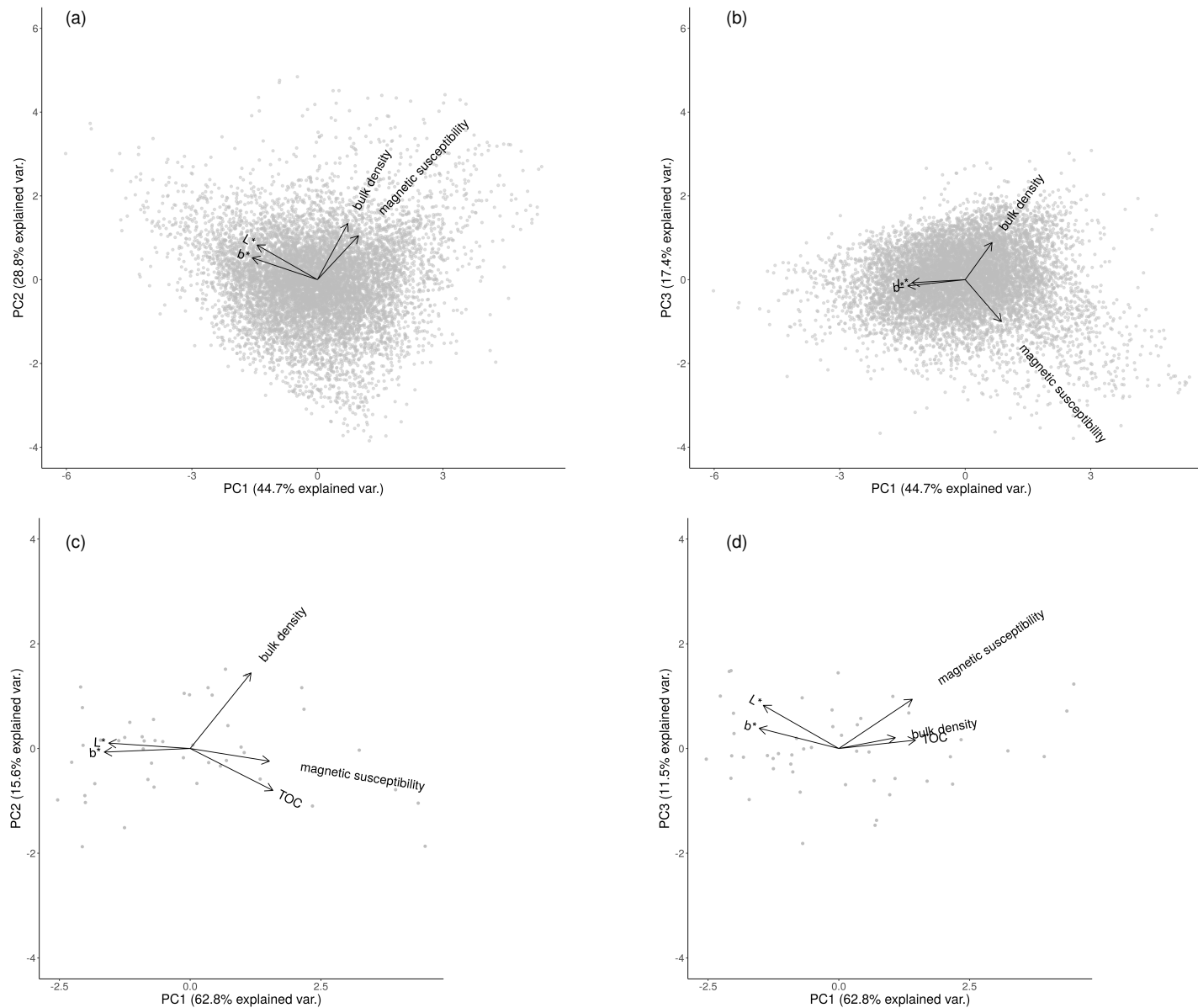
The two younger $^{40}\text{Ar}/^{39}\text{Ar}$ dates (samples V14 and V2A) are identical within 2σ errors, and are assumed to date the same event (i.e., the formation of the maar). The older date (sample V15) does not overlap within 2σ errors with either of the younger dates, therefore this sample is assumed to be a reworked volcanic clast. The inverse-variance weighted mean $^{40}\text{Ar}/^{39}\text{Ar}$ date of the option ^c ages and errors from the two youngest basalt samples is 23.29 ± 0.32 Ma (2σ ; with an acceptable Mean Square Weighted Deviation (MSWD) value of 0.42). This date defines the interval when the magnetic reversal at the base of core FH2 occurred, which is now 23.61–22.97 Ma. Although this interval is longer than that used in Fox et al. (2016), it does not include any reverse → normal magnetic reversals that have not already been considered in that study. We

therefore conclude that the previously published age model is robust and is not changed by the use of internal as well as external $^{40}\text{Ar}/^{39}\text{Ar}$ errors.

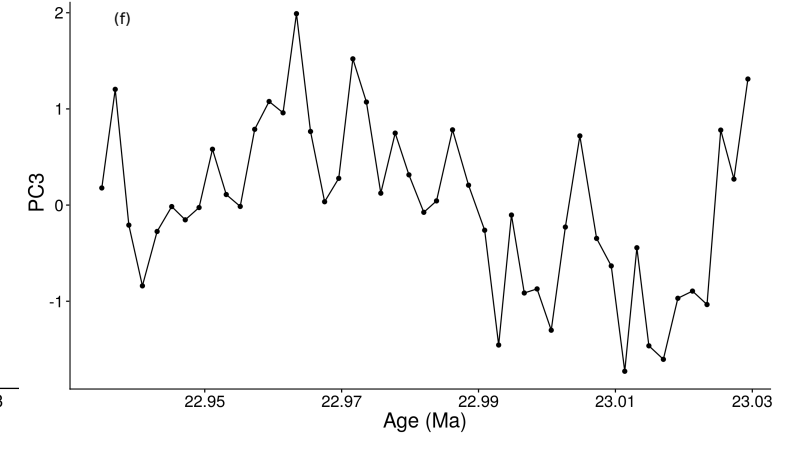
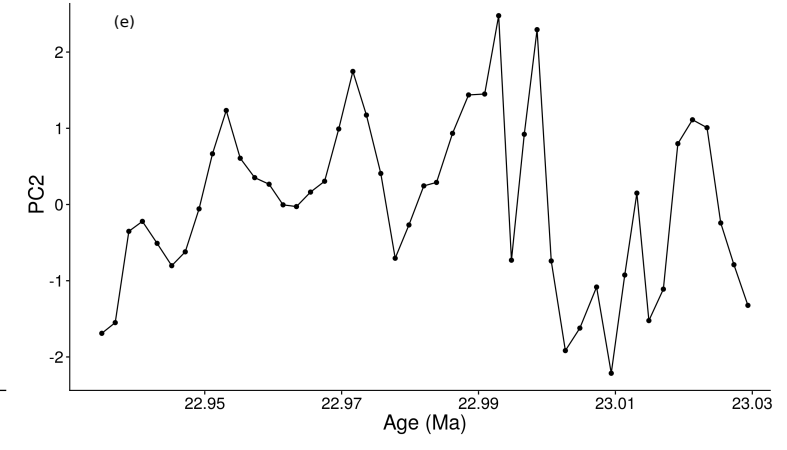
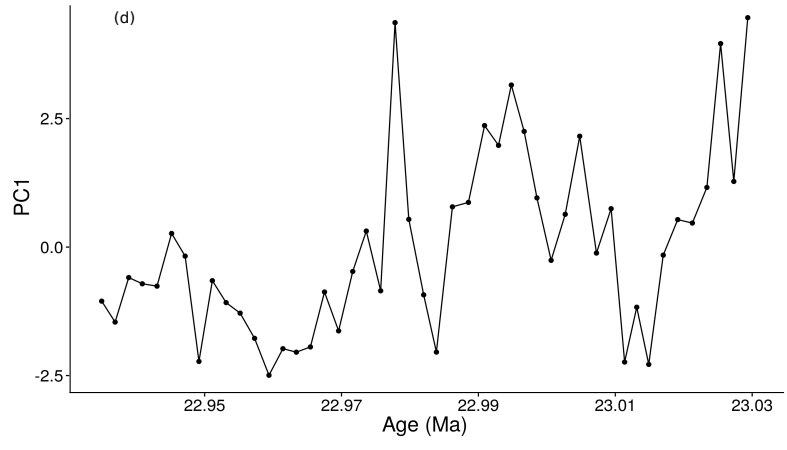
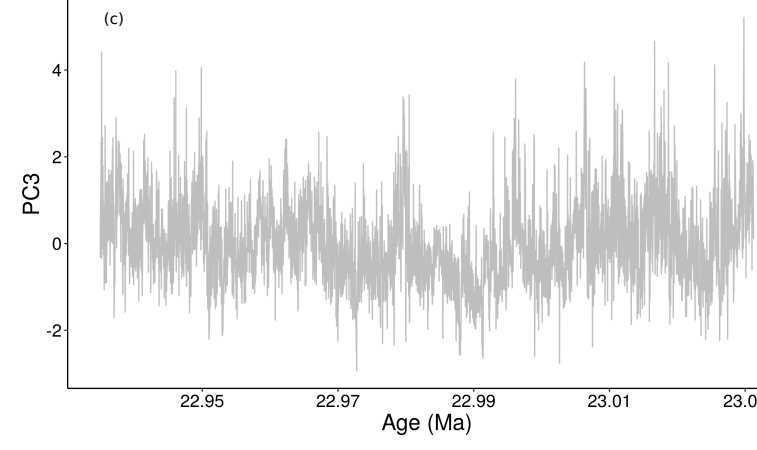
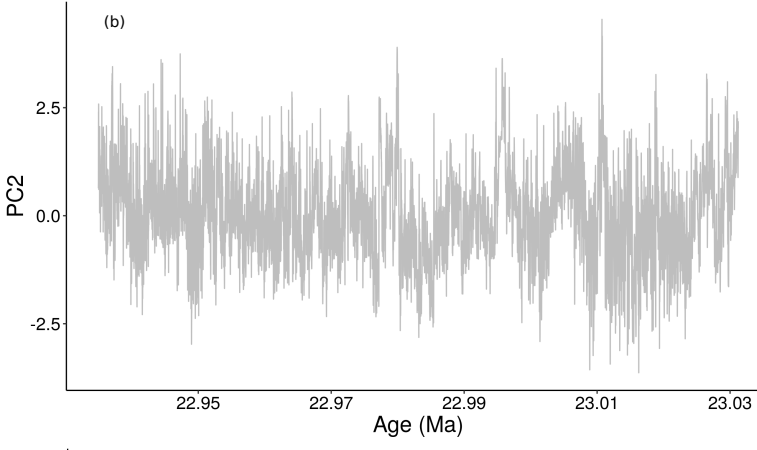
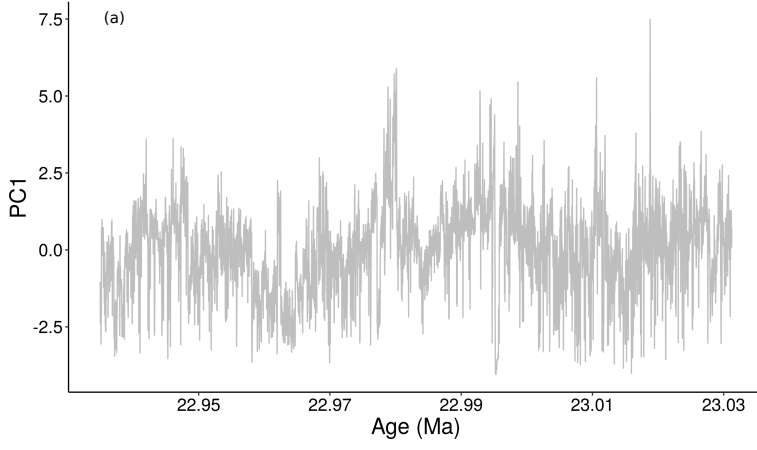
2. Supplementary figures.



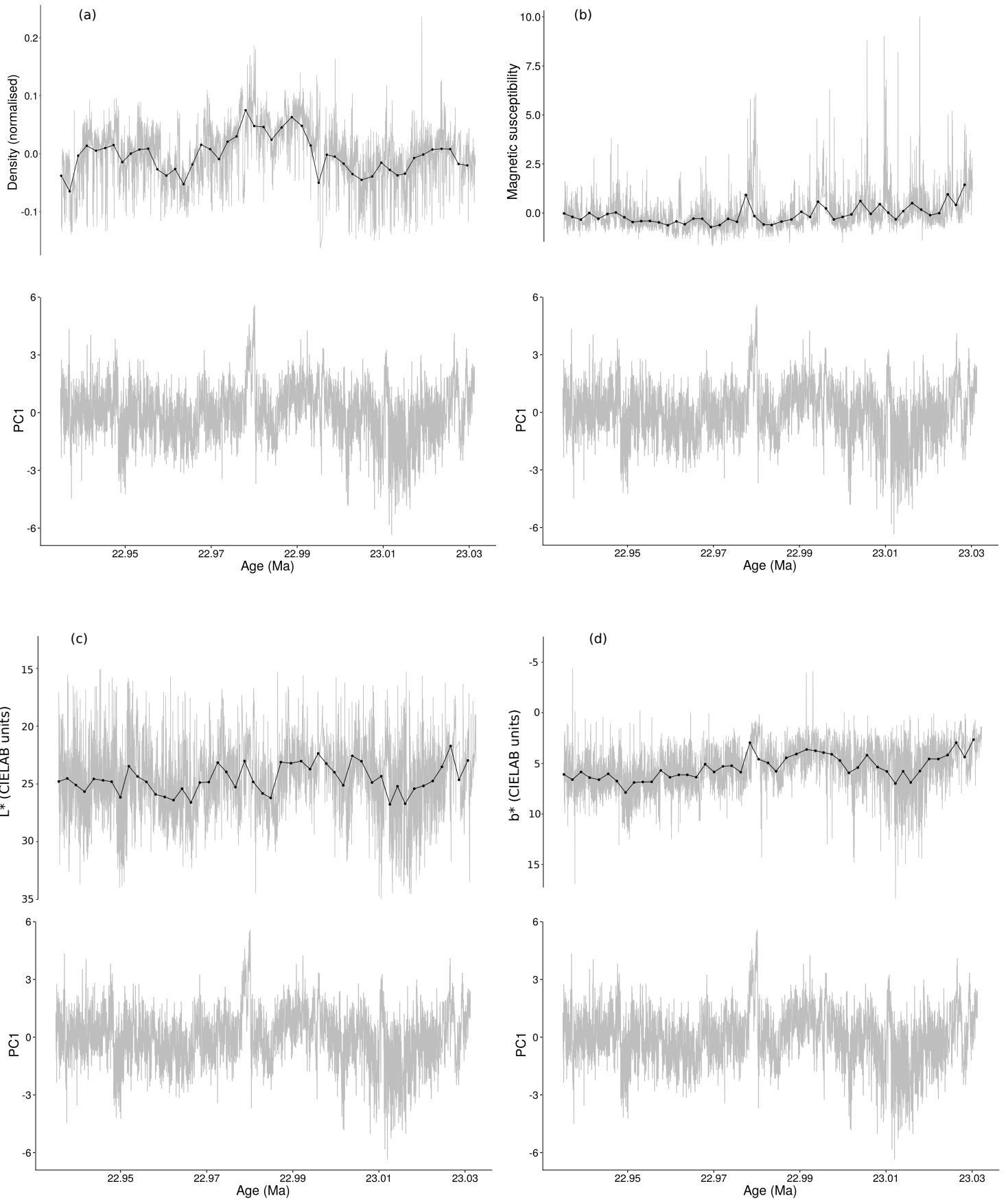
Supplementary Figure 1: Unmodified density data. Note step at ~ 22.991 Ma. Grey line is full dataset, black line is resampled dataset.



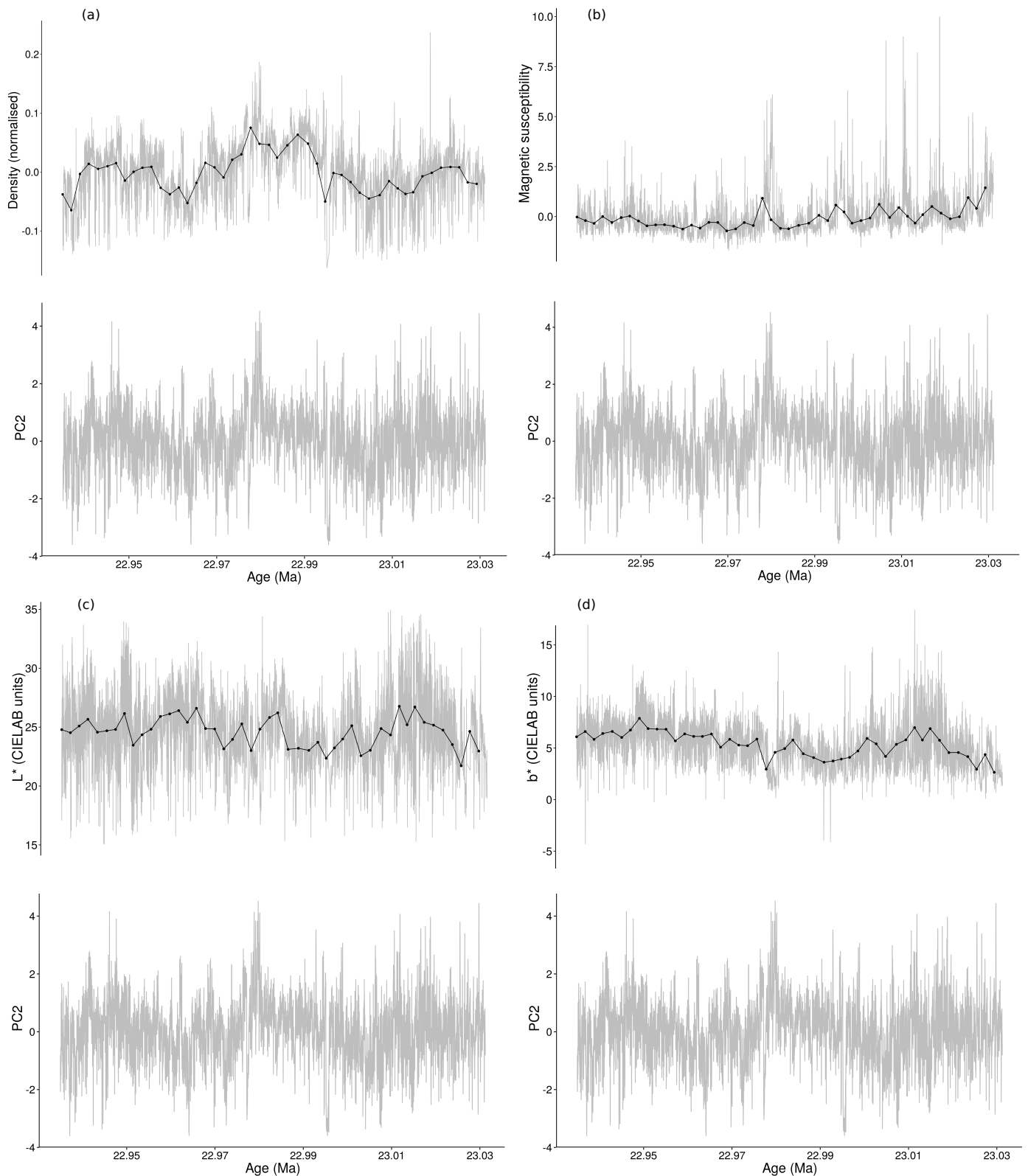
Supplementary Figure 2: Principal component analysis performed using the unmodified density dataset shown in Supplementary Figure 1. There is very little difference between these results and those shown in Figure 6. (a) Full dataset, principal components (PCs) 1 and 2; (b) full dataset, PCs 1 and 3; (c) resampled dataset, PCs 1 and 2; (d) full dataset, PCs 1 and 3.



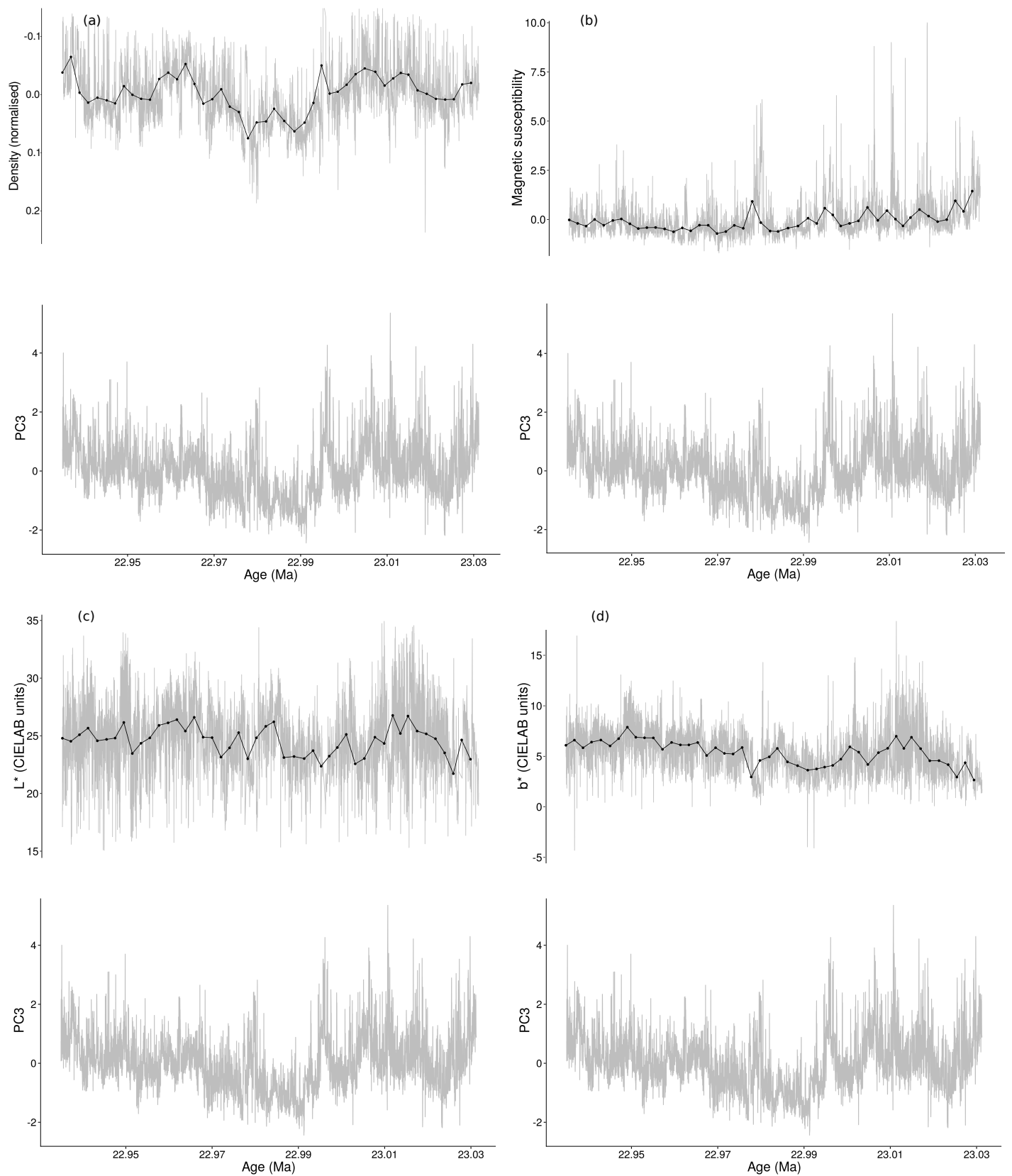
Supplementary Figure 3: Reconstructed PCs 1, 2 and 3 for the full dataset (a-c) and the resampled dataset (d-f) using the unmodified density data shown in Supplementary Figure 1.



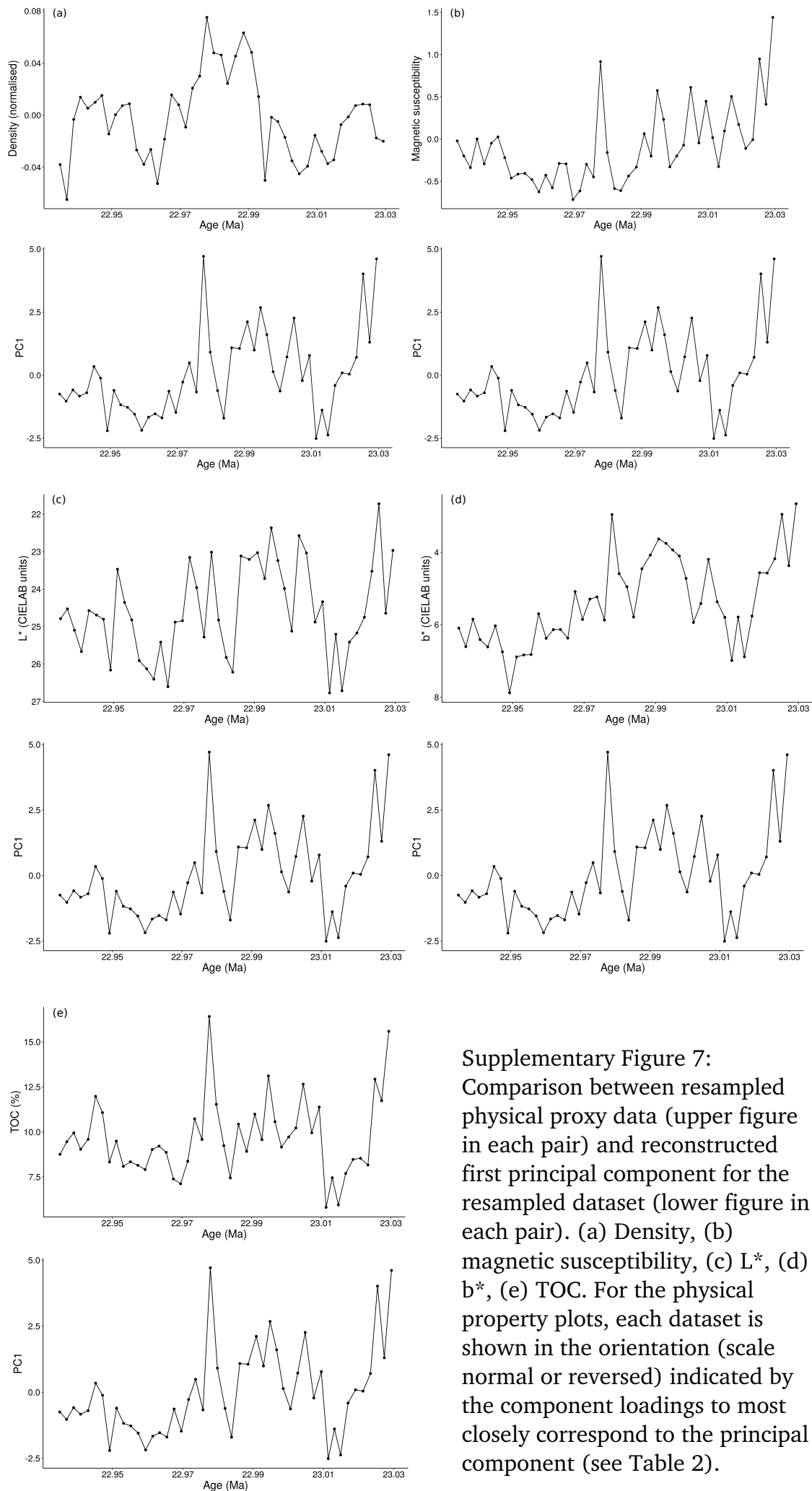
Supplementary Figure 4: Comparison between full and resampled physical proxy data (upper figure in each pair) and reconstructed first principal component for the full dataset (lower figure in each pair). (a) Density, (b) magnetic susceptibility, (c) L*, (d) b*. Grey lines are full dataset, black lines in upper figures represent the resampled dataset. For the physical property plots, each dataset is shown in the orientation (scale normal or reversed) indicated by the component loadings to most closely correspond to the principal component (see Table 2).



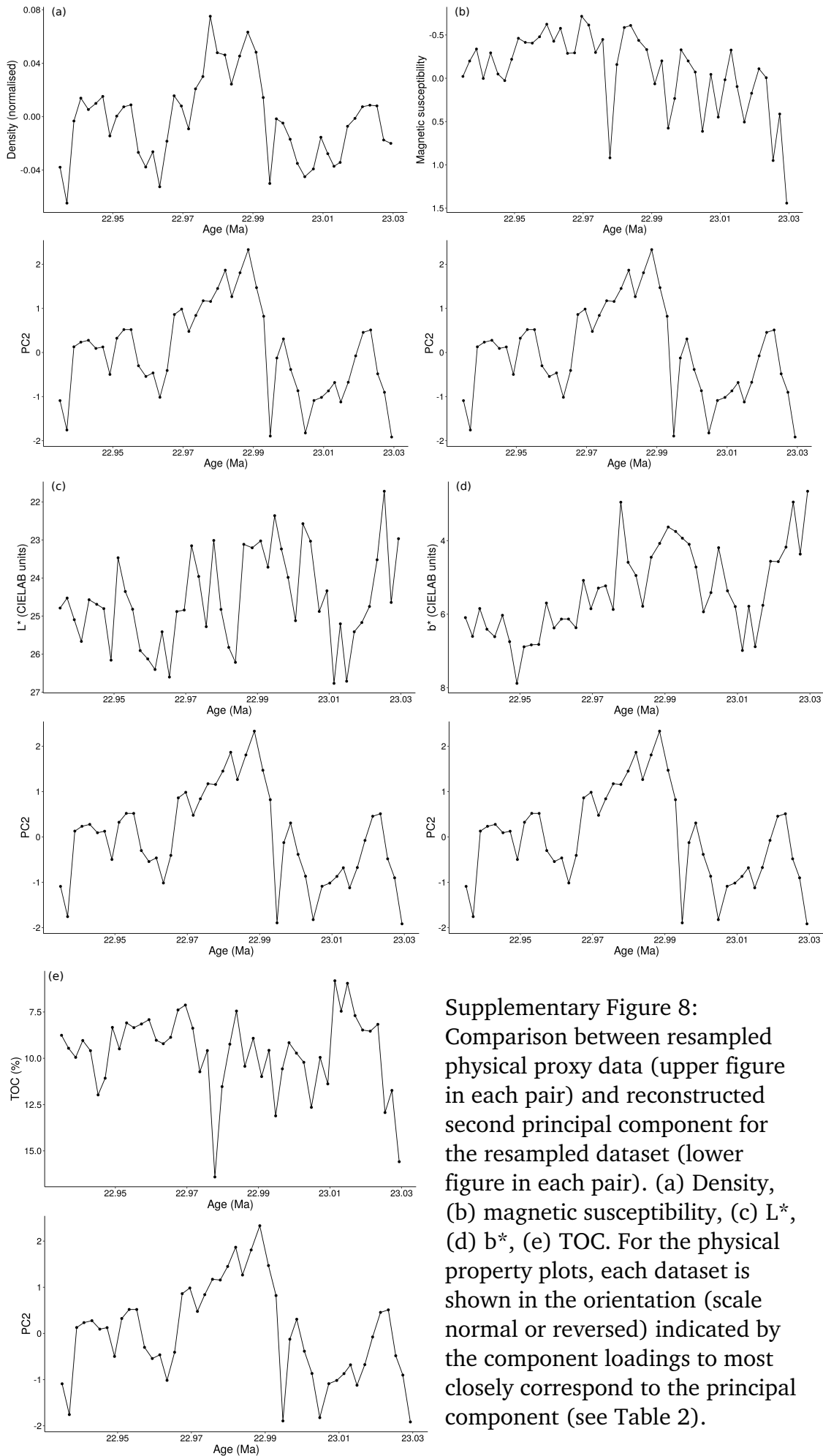
Supplementary Figure 5: Comparison between full and resampled physical proxy data (upper figure in each pair) and reconstructed second principal component for the full dataset (lower figure in each pair). (a) Density, (b) magnetic susceptibility, (c) L^* , (d) b^* . Grey lines are full dataset, black lines in upper figures represent the resampled dataset. For the physical property plots, each dataset is shown in the orientation (scale normal or reversed) indicated by the component loadings to most closely correspond to the principal component (see Table 2).



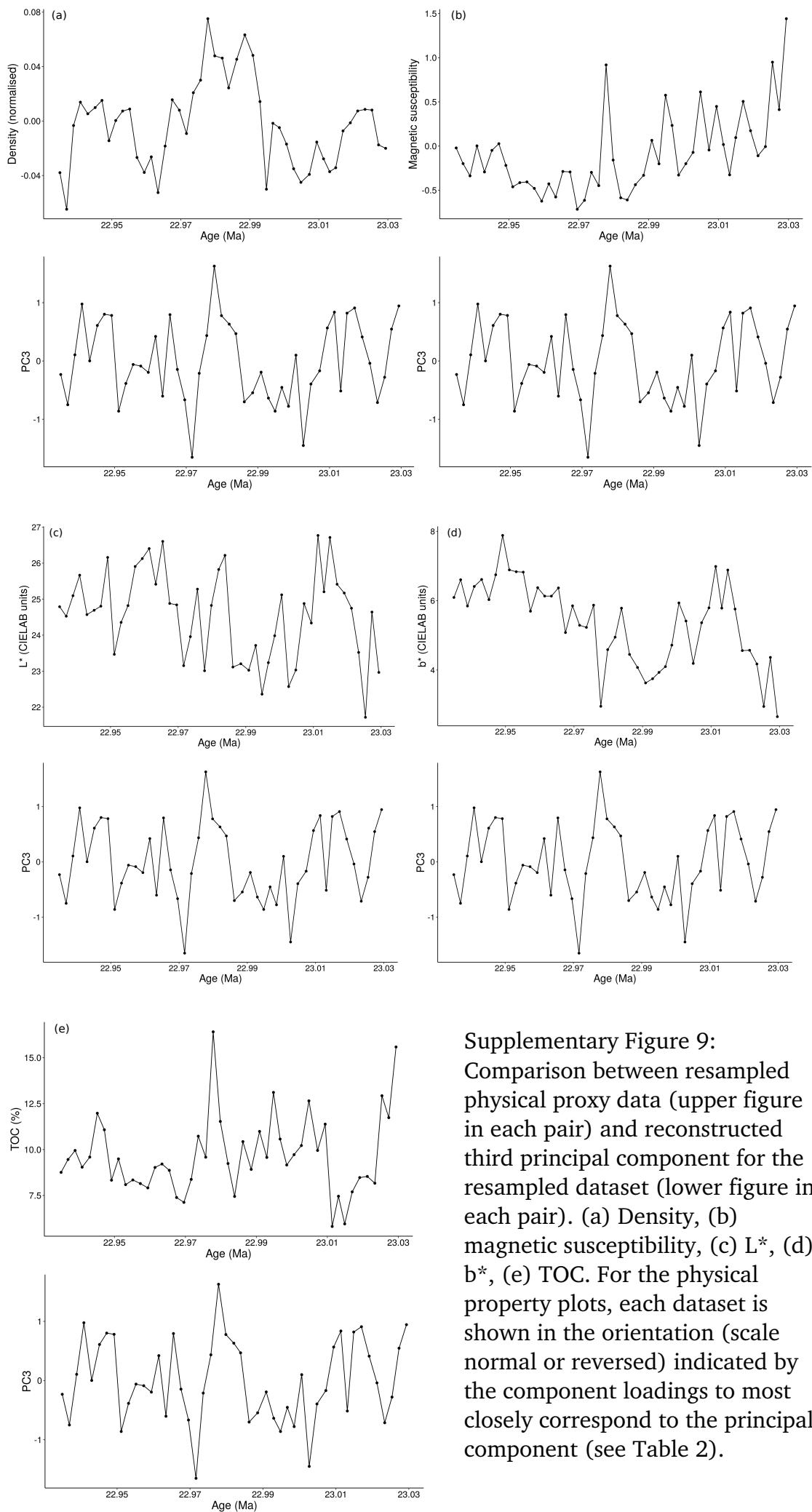
Supplementary Figure 6: Comparison between full and resampled physical proxy data (upper figure in each pair) and reconstructed third principal component for the full dataset (lower figure in each pair). (a) Density, (b) magnetic susceptibility, (c) L^* , (d) b^* . Grey lines are full dataset, black lines in upper figures represent the resampled dataset. For the physical property plots, each dataset is shown in the orientation (scale normal or reversed) indicated by the component loadings to most closely correspond to the principal component (see Table 2).



Supplementary Figure 7:
Comparison between resampled physical proxy data (upper figure in each pair) and reconstructed first principal component for the resampled dataset (lower figure in each pair). (a) Density, (b) magnetic susceptibility, (c) L*, (d) b*, (e) TOC. For the physical property plots, each dataset is shown in the orientation (scale normal or reversed) indicated by the component loadings to most closely correspond to the principal component (see Table 2).



Supplementary Figure 8:
Comparison between resampled physical proxy data (upper figure in each pair) and reconstructed second principal component for the resampled dataset (lower figure in each pair). (a) Density, (b) magnetic susceptibility, (c) L*, (d) b*, (e) TOC. For the physical property plots, each dataset is shown in the orientation (scale normal or reversed) indicated by the component loadings to most closely correspond to the principal component (see Table 2).



Supplementary Figure 9:
Comparison between resampled physical proxy data (upper figure in each pair) and reconstructed third principal component for the resampled dataset (lower figure in each pair). (a) Density, (b) magnetic susceptibility, (c) L*, (d) b*, (e) TOC. For the physical property plots, each dataset is shown in the orientation (scale normal or reversed) indicated by the component loadings to most closely correspond to the principal component (see Table 2).

3. References

- Beckinsale, R.D. and Gale, N.H., 1969, A reappraisal of the decay constants and branching ratio of ^{40}K : *Earth and Planetary Science Letters*, v. 6, p. 289–294.
- Fox, B. R. S., Wartho, J., Wilson, G. S., Lee, D. E., Nelson, F. E., and Kaulfuss, U., 2015, Long-term evolution of an Oligocene/Miocene maar lake from Otago, New Zealand: *Geochemistry, Geophysics, Geosystems*, v. 16, p. 59–76, doi: 10.1002/2014GC005534.
- Fox, B. R. S., Wilson, G. S., and Lee, D. E., 2016, A unique annually laminated maar lake sediment record shows orbital control of Southern Hemisphere midlatitude climate across the Oligocene-Miocene boundary: *Geological Society of America Bulletin*, March 2016, v. 128, p. 609–626.
- Garner, E.L., Murphy, T.J., Gramlich, J.W., Paulsen, P.J., and Barnes, I.L., 1975, Absolute isotopic abundance ratios and the atomic weight of a reference sample of potassium: *Journal of Research of the National Bureau of Standards*, v. 79A, p. 713–725.
- Koppers, A.A.P, 2002, ArArCALC software for $^{40}\text{Ar}/^{39}\text{Ar}$ age calculations: *Computers and Geosciences*, v. 28, p. 605–619.
- Kuiper, K.F., Deino, A., Hilgen, F.J., Krijgsman, W., Renne, P.R., and Wijbrans, J.R., 2008, Synchronizing rock clocks of Earth history: *Science*, v. 320, p. 500–504.
- Lanphere, M.A. and Dalrymple, G.B., 2000, First-principles calibration of ^{38}Ar tracers: Implications for the ages of $^{40}\text{Ar}/^{38}\text{Ar}$ fluence monitors, US Geological Survey professional paper, no. 1621, p. 1–10.
- Min, K., Mundil, R., Renne, P.R., and Ludwig, K.R., 2000, A test for systematic errors in $^{40}\text{Ar}/^{39}\text{Ar}$ geochronology through comparison with U/Pb analysis of a 1.1-Ga rhyolite: *Geochimica et Cosmochimica Acta*, v. 64, p. 73–98.
- Renne, P.R., Swisher, C.C., Deino, A.L., Karner, D.B., Owens, T.L., and DePaolo, D J., 1998, Intercalibration of standards, absolute ages and uncertainties in $^{40}\text{Ar}/^{39}\text{Ar}$ dating: *Chemical Geology*, v. 145, p. 117–152.
- Schwarz, W.H. and Trieloff, M., 2007, Intercalibration of $^{40}\text{Ar}-^{39}\text{Ar}$ age standards NL-25, HB3gr hornblende, GA1550, SB-3, HD-B1 biotite and Bmus/2 muscovite: *Chemical Geology*, v. 242, p. 218–231.
- Steiger, R.H. and Jäger, E., 1977, Subcommittee on geochronology: Convention on the use of decay constants in geo- and cosmochronology, *Earth and Planetary Science Letters*, v. 36, p. 359–362.
- Timm, C., Hoernle, K., Werner, R., Hauff, F., van den Bogaard, P., White, J., Mortimer, N., and Garbe-Schöberg, D., 2010, Temporal and geochemical evolution of the Cenozoic intraplate volcanism of Zealandia, *Earth-Science Reviews*, v. 98, p. 38–64.